Seismic wavefield imaging of Earth's interior across scales

Jeroen Tromp

Abstract | Seismic full-waveform inversion (FWI) for imaging Earth's interior was introduced in the late 1970s. Its ultimate goal is to use all of the information in a seismogram to understand the structure and dynamics of Earth, such as hydrocarbon reservoirs, the nature of hotspots and the forces behind plate motions and earthquakes. Thanks to developments in high-performance computing and advances in modern numerical methods in the past 10 years, 3D FWI has become feasible for a wide range of applications and is currently used across nine orders of magnitude in frequency and wavelength. A typical FWI workflow includes selecting seismic sources and a starting model, conducting forward simulations, calculating and evaluating the misfit, and optimizing the simulated model until the observed and modelled seismograms converge on a single model. This method has revealed Pleistocene ice scrapes beneath a gas cloud in the Valhall oil field, overthrusted Iberian crust in the western Pyrenees mountains, deep slabs in subduction zones throughout the world and the shape of the African superplume. The increased use of multi-parameter inversions, improved computational and algorithmic efficiency, and the inclusion of Bayesian statistics in the optimization process all stand to substantially improve FWI, overcoming current computational or data-quality constraints. In this Technical Review, FWI methods and applications in controlled-source and earthquake seismology are discussed, followed by a perspective on the future of FWI, which will ultimately result in increased insight into the physics and chemistry of Earth's interior.

Body waves
Seismic waves that travel through Earth's interior as compressional or shear waves.

Surface waves
Seismic waves that rumble along Earth's surface in the form of a Love wave with transverse linear particle motion or a Rayleigh wave with vertical and radial retrograde elliptical particle motion.

Department of Geosciences and the Program in Applied & Computational Mathematics, Princeton University, Princeton, NJ, USA.

e-mail: jtromp@princeton.edu

https://doi.org/10.1038/s43017-019-0003-8

Seismic waves are generated by a wide variety of mechanisms, including earthquakes, man-made 'controlled' sources and wind, ocean and environmental noise. Time series of seismic waves (seismograms) are recorded by seismographic instruments, such as permanent, three-component broadband seismometers in regional and global networks, temporary arrays deployed on land and the seafloor, towed arrays of hydrophones in offshore exploration and arrays of geophones in onshore exploration. Analyses of seismograms enable researchers to glean information about Earth's structure and the nature of seismic sources. However, traditional analyses — based on the arrival times of body waves or the dispersion measurements of surface waves — sometimes yield inconclusive results.

To the first approximation, Earth can be regarded as spherically symmetric on a global scale or as flat and horizontally layered on a local scale. In such laterally homogeneous models, it is easy to calculate the expected arrival times and waveforms of seismic waves, for example, the first-arriving body waves, which are compressional (P) waves and secondary shear (S) waves, or the waveforms of long-period (>~90 s) dispersed surface waves. Calculated travel times and waveforms often closely resemble observations, and differences between calculated and observed values can be used to constrain Earth's lateral variations.

In classical body-wave seismology, information in seismograms is reduced to a few select travel-time 'picks'; entire catalogues of such picks are available from the International Seismological Centre. Similarly, classical surface-wave seismology focuses on the dispersion of waves travelling along Earth's surface, which help to constrain crust and upper mantle heterogeneity. In classical exploration seismology, distinct wave arrivals recorded at the surface are geometrically traced to their origin in the subsurface, creating 'migrated' images of the structure targeted by the seismic survey. The analysis of this type of information is generally based on simplified theories of seismic-wave propagation (for example, ray theory), which are computationally inexpensive, thereby enabling the analysis of large data sets. These underlying approaches are simple and powerful, and have led to ground-breaking images of Earth's interior on all scales[1–6].

Classical methods fail when Earth can no longer be considered homogenously layered. For instance, Earth's crust varies in thickness by an order of magnitude,

Key points

- Modern numerical methods and high-performance computers have facilitated the characterization of Earth's interior constrained by the physics of seismic-wave propagation.
- Seismic full-waveform inversion (FWI) has enabled unprecedented imaging across nine orders of magnitude in frequency and wavelength, with applications ranging from medical imaging and nondestructive testing to global seismology.
- FWI continues to be developed and improved, with opportunities for a more complete description of the physics of seismic-wave propagation (for example, anisotropy, attenuation and poroelasticity), as well as better and more effective optimization algorithms (such as source encoding, uncertainty quantification and Hamiltonian Monte Carlo methods).
- Computers in the exascale era (~2020–2021) will enable global FWI at frequencies of up to ~1 Hz, potentially facilitating sub-10-km-scale imaging of Earth's mantle.

from ~7 km underneath the oceans to ~70 km beneath the Andes and Tibet[7,8]. As another example, the Gulf of Mexico contains high-wave-speed salt domes with complex geometries embedded in slow-wave-speed sediments[9], and this type of environment cannot be modelled based on theories that invoke perturbations to smooth 'background' models. The goal of seismic full-waveform inversion (FWI) is to use all information contained in seismographic recordings — that is, every wiggle in a seismogram — to determine the structure of Earth's interior, constrained by the physics of seismic-wave propagation. This approach embraces the complexity of 3D seismic-wave propagation, thereby enabling seismic imaging of Earth's interior across scales, even in complex environments that cannot be approximated by simple models.

FWI is computationally and algorithmically demanding, and, although these demands hampered progress for many decades, these restrictions have been largely overcome in the past decade, due to advances in algorithms and computing technology. Today, FWI is widely used in applications including medical imaging[10–14], nondestructive testing[15–24], near-surface characterization[25–30], onshore and offshore exploration seismology[31–39], deep crustal seismic imaging[40–47], earthquake seismology[48–54] and ambient-noise seismology[55,56]. A comprehensive overview of FWI in exploration seismology was presented by Virieux and Operto[57], and Fichtner[58] and Liu and Gu[59] gave overviews of elastic-waveform inversion.

In this Technical Review, the history and goals of FWI are first briefly discussed. The FWI process is then explained, followed by examples of applications of FWI in controlled-source and earthquake seismology. Finally, current challenges and opportunities for advancement in FWI are highlighted.

Brief history

The ambition to constrain the structure of Earth's interior using complete seismic-wave propagation physics dates back to the early 1980s (FIG. 1). Bamberger et al.[60], Lailly[61] and Tarantola[62] formulated and adapted the adjoint-state method[63,64] to address inverse problems in exploration seismology in a process reminiscent of data-assimilation methods widely used in fluid mechanics[65,66]. This approach enabled the gradient of a predefined misfit function to be calculated with respect to a chosen set of model parameters. This was based on the convolution of a 'forward' wavefield generated by a seismic source with a fictitious 'adjoint' wavefield generated by injecting time-reversed differences between observed and simulated seismograms simultaneously at all receivers. The calculated misfit gradient is then used to iteratively update the model parameters until a local minimum of the misfit function has been reached. Despite modest early success[31–33], it was not until the 1990s that what is now referred to as FWI was successfully applied[34–38], and in 2007, a breakthrough came as a successful blind inversion test[39], which applied 2D acoustic-waveform tomography using third-party elastic-wave-equation data to recover crustal compressional wave speeds.

In earthquake seismology, early ideas for waveform inversion in spherically symmetric background models originated with Woodhouse and Dziewoński[3], who modelled mantle waves based on the 'path-average' or 'great-circle' approximation, and Nolet[67–69], who inverted the fundamental-mode surface wavefield based on 'partitioned waveform inversion'. Li and Tanimoto[70] modelled the broadband body-wave field based on the Born approximation, and Li and Romanowicz[71,72] generalized this approach based on a nonlinear asymptotic coupling theory (NACT).

In the early 2000s, the finite-frequency 'banana-doughnut' version of classical (infinite-frequency) ray theory was developed[73–76] and later connections[77–80] between banana-doughnut theory and the adjoint-state method[81] were drawn. FWI was finally applied on the continental scale in the late 2000s, when the southern California crust[48–50] and the upper-mantle structure in the Australasian region[51,52] were imaged. More than 30 years after waveform inversion was invented, the first 3D global models based on this ambitious idea were produced[53,54].

Full-waveform inversion

The goal of FWI is to match simulated seismograms to observed seismograms by iteratively constructing a model of Earth's interior (FIG. 2). Here, the selection of seismic sources and starting models, forward simulations, calculation of the misfit function, adjoint simulations and optimization are described. FWI is then compared with 'classical' Earth-imaging methods.

Seismic sources. The FWI process starts with the selection of a set of seismic sources, which are earthquakes in regional and global seismology, and controlled sources in the form of airguns offshore and vibrators or explosions onshore in exploration seismology. A data set of observed seismograms is then constructed by gathering data from all relevant seismographic stations or hydrophone or geophone arrays. Next, a complementary set of simulated or 'synthetic' seismograms are calculated by numerically solving the partial differential equation (PDE) that governs seismic-wave propagation. This makes FWI a PDE-constrained optimization problem[82,83], because the model parameters constrained by the optimization process also control the PDE. There are two parameters for acoustic waves, the sound wave

Misfit function
A multivariate function of a set of model parameters indicative of the fit between observed and simulated data.

Mantle waves
Very-long-period (> ~ 120 s) surface waves.

Forward simulations
Numerical modelling of seismic-wave propagation given a set of source parameters and an Earth model.

Adjoint simulations
Numerical modelling based on an Earth model and a fictitious set of sources that inject measurements simultaneously from all receivers.

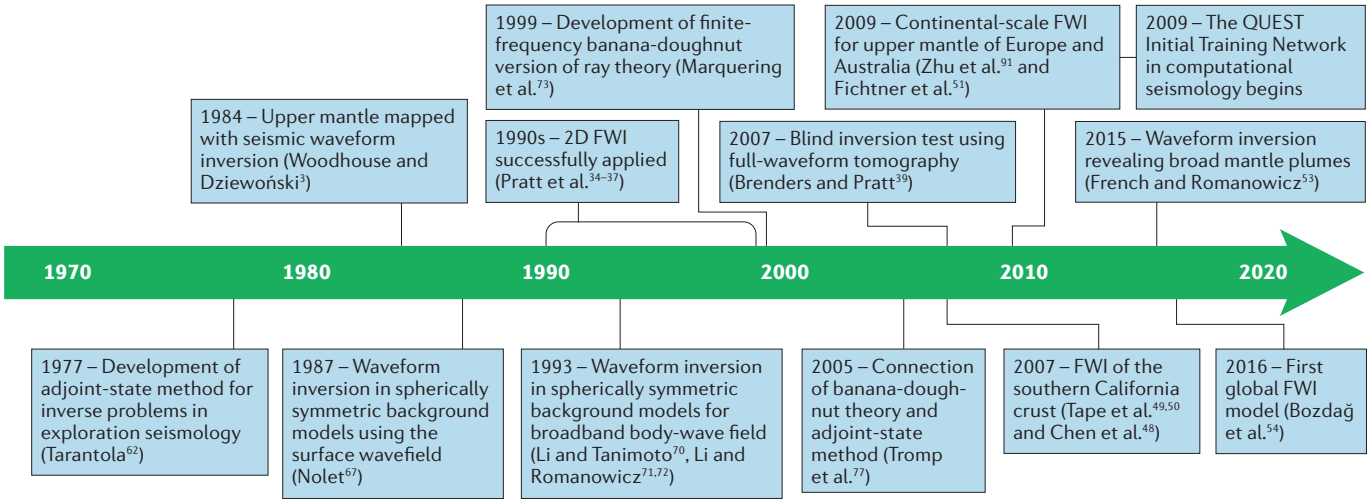

Fig. 1 | **Timeline of major developments in seismic FWI and notable applications.** Major developments in seismic full-waveform inversion (FWI) are illustrated from its inception in 1977 to current applications. Classical inversion methods utilizing seismic waveforms are referred to as 'waveform inversion' to distinguish such approaches from FWIs based on the adjoint-state method.

speed and the mass density, and three for isotropic elastic waves, the mass density and the compressional and shear wave speeds. Additional model parameters can be included to account for complexities such as attenuation, anisotropy and source parameters. In practice, the time windows that are used in FWI are only those in which observed and simulated seismograms are sufficiently similar to make reliable measurements. For example, the first-arriving waves in a shot gather or specific body-wave or surface-wave arrivals, and frequently something other than simple waveform differences are measured, for example differences in phase or amplitude. Thus, the term FWI can be an overstatement, because neither the full physics of wave propagation nor complete broadband seismograms are generally employed.

Starting model. The calculation of synthetic seismograms for comparison with observed data requires a suitably chosen starting model. In earthquake seismology, selecting the starting model is relatively straightforward, as the basic 1D (radial) structure of the Earth has been known for decades[84] and current 3D global seismic models are in general agreement in terms of long-wavelength heterogeneity, regardless of data type and inversion strategy[85–88]. However, in exploration seismology, determining a good starting model can be highly nontrivial; if the initial set of synthetic seismograms fails to match any aspect of the observed data to within a half-cycle, the FWI process is likely to fail. One way to mitigate such failure is to initiate FWI with relatively low-frequency waves before slowly blending in higher frequencies[89]. This is readily accomplished in earthquake seismology by selecting large earthquakes and using long-period (>~90 s) waves that 'see' relatively long-wavelength heterogeneities[54,90,91]. However, in exploration seismology, it is generally difficult to generate low-frequency waves. Nevertheless, extensive use of ocean-bottom nodes has enabled long-wave (2–2.5 Hz) data extraction in offshore exploration and coupling of vibrators has enabled the generation of 1.5-Hz data in onshore exploration[92].

Forward simulations. Given a starting model and a set of source parameters, forward simulations are used to calculate synthetic seismograms for all seismic sources in the database. This process involves numerical simulations of controlled sources recorded by arrays of geophones (onshore) or hydrophones and ocean-bottom instruments (offshore) in exploration seismology, and simulations of earthquakes recorded by the Global Seismographic Network (GSN) and regional arrays (for example, USArray, F-net, Hi-net and MedNet) in earthquake seismology. A requirement for practical FWI is a fast, scalable seismic-wave propagation solver to calculate the 'forward' wavefield, resulting in synthetic seismograms at all the receivers, and this can be achieved through various numerical methods[93].

Traditionally, industry has used time-domain finite-difference methods[94–96] based on acoustic applications. Seismic data are often acquired in an offshore environment with seismic sources and receivers located in the water layer, explaining why FWI was originally developed in the acoustic approximation in the time dom ain[31,32,62,97,98]. In the 1990s, a frequency-domain approach was introduced with initial applications to crosshole data and subsequently to wide-aperture surface seismic data[34,36,99], thereby focusing on easier-to-model transmitted rather than reflected waves. Today, both time-domain and frequency-domain algorithms remain popular for acoustic and elastic applications.

In contrast to industry, earthquake seismologists have focused exclusively on the (an)elastic case because shear waves and surface waves are integral parts of the earthquake-generated wavefield. Here, time-domain solvers based on the spectral-element method[100–104] are heavily favoured because of their ability to accommodate topography, bathymetry and fluid–solid boundaries, such as the core–mantle boundary (CMB),

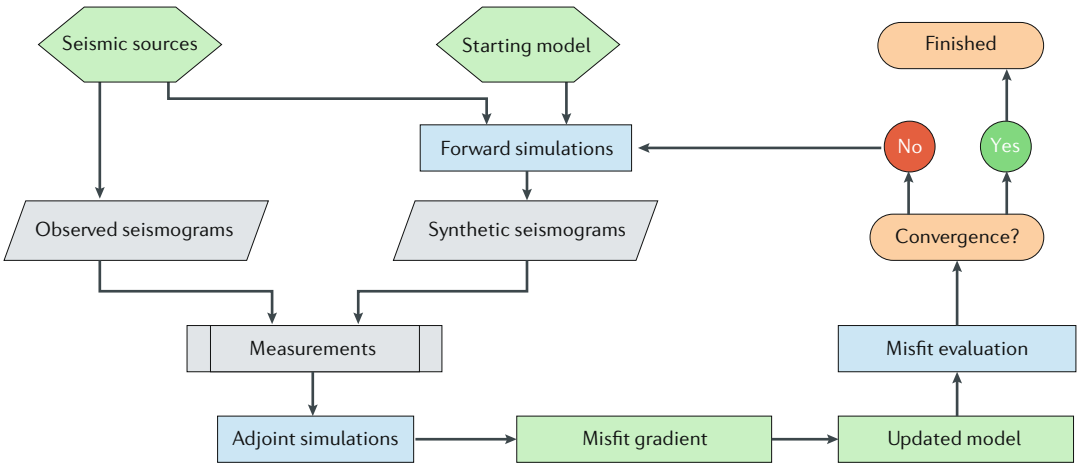

Fig. 2 | **FWI workflow.** The full-waveform inversion (FWI) process is initiated by choosing a collection of seismic sources and a starting model, both of which are required for the calculation of synthetic seismograms based on 'forward' simulations. For each seismic source, synthetic seismograms are compared with corresponding observed seismograms by measuring their differences, which, collectively, define a misfit function. These measurements drive 'adjoint' simulations, which, one source at a time, are combined to obtain the gradient of the misfit function with respect to the model parameters. This gradient, or 'Fréchet derivative', is used to update the starting model, resulting in a reduction of the misfit. This optimization process is iterated until the inversion has reached the minimum of the chosen misfit function. The green boxes denote tasks involving model parameters, the light blue boxes denote tasks involving significant numerical simulations and the grey boxes denote tasks that involve time-series processing and analysis.

thereby accurately capturing dispersive surface waves and diffracted waves.

Misfit function. Following forward simulations, the observed and simulated seismograms must be compared, requiring the selection and use of a misfit function. In its simplest form, the misfit function sums the least-squares difference between observed and simulated seismograms for a chosen duration of time and frequency band. However, it is important to recognize that any type of misfit function can be selected, and its nature is determined by what measurement is used to determine the difference between the observed and simulated data. For example, if the misfit is not a Gaussian distribution[105], such as when there are large outliers, misfit criteria other than a least-squares difference, for example based on an L1 norm, should be considered[98,106]. Alternative or multiple measurements can also be used; for example, travel-time anomalies for specific seismic arrivals (such as the P or S wave) can be used[77]. Other potential measurements include frequency-dependent phase and amplitude anomalies[107,108], surface-wave dispersion[109], (instantaneous) phase or waveform envelopes[110,111] or 'double-difference' versions of any of these measurements[112], that is, differencing differential measurements between pairs of stations recording the same earthquake. Sometimes, selecting the right misfit measurement holds the key to unlocking certain model parameters. For instance, a distinct characteristic of seismic anisotropy is that it 'splits' the arrival times of horizontally and vertically polarized shear waves; therefore, measuring this S-wave splitting provides direct constraints on anisotropic model parameters. Generally, inversions in earthquake seismology focus almost exclusively on using misfit functions that fit phase information in distinct time windows, disregarding amplitude information for reasons of source uncertainty, inadequate instrument response information and contamination owing to site effects. As some amplitude information is disregarded, earthquake seismologists do not currently employ FWI sensu stricto.

In exploration seismology, straight waveform differences of first-arriving waves are generally used in the misfit function, but other methods have been developed. For instance, a logarithmic misfit function was introduced[113,114] and used to investigated FWI in the Laplace and Laplace–Fourier domains[115,116]. The latter is equivalent to performing an inversion of a wavefield damped in time, partially suppressing dispersive surface waves that are difficult to fit. The cycle-skipping problem[106,117,118], in which observed and simulated waveforms are misaligned by one cycle or more, renders incorrect misfit measurements and hinders convergence. This issue has motivated reformulations of the inverse problem that are less sensitive to cycle skipping, including adaptive waveform inversion[117], source-receiver extension[119], extension through time lag[120], the use of optimal transport distance[106,121–123] and wavefield-reconstruction inversion[124,125].

Adjoint simulations. The objective of the inversion process is to minimize a chosen misfit function (FIG. 2). In FWI, this is accomplished by using the adjoint-state method[63,64,81] to calculate the gradient of the misfit with respect to the model parameters, and then using the gradient to steadily reduce the misfit. To do this with adjoint simulations, misfit measurements are simultaneously injected in reverse time at all the receivers that recorded a given event. This distributed 'adjoint source' gives rise to an 'adjoint wavefield' and the interaction between this wavefield and the regular forward wavefield 'paints' the Fréchet derivatives[77,78]. These are model

Fréchet derivatives
The derivatives of a misfit function with respect to model parameters, such as seismic wave speeds or source parameters.

parameter gradients, known as 'kernels', that generalize the derivative of a single variable function to the derivative of a function with respect to another function (that is, a functional derivative). Every measurement has its own unique associated Fréchet derivative[111] or misfit gradient. In other words, the kernels reflect the measurements. For example, traditional cross-correlation travel-time anomaly measurements have Fréchet derivatives that correspond exactly to finite-frequency banana-doughnut kernels[73,77]. However, obtaining the Fréchet derivatives through the convolution of the forward and adjoint fields can be challenging in the presence of attenuation[126,127] because the data volumes associated with these wavefields are considerable. The computational cost of adjoint-state calculations[60–62] is independent of the number of model parameters and the number of receivers, initially prompting the development of FWI in exploration seismology. Although that field uses both time-domain[128] and frequency-domain[129–131] implementations of these simulations, time-domain spectral-element solvers are preferred in earthquake seismology[100,104,132,133]. These solvers use an 'optimize-then-discretize' approach to the adjoint operator[134].

Optimization. Current FWI algorithms rely on steepest descent, conjugate gradient, Newton, Gauss–Newton or quasi-Newton methods to iteratively reduce, or optimize, the misfit[57,135–139]. Today, the most popular method is the limited-memory Broyden–Fletcher–Goldfarb–Shanno (L-BFGS) algorithm[140–142], which is generally regarded as the most effective quasi-Newton method[143]. However, the problem with all of these local optimization methods is the assumption that they converge to the global minimum of the misfit function. Unfortunately, the misfit function may have local minima, and local optimization may fail to converge to the global minimum, owing to, for instance, a poor starting model, a lack of low-frequency data, poor-quality data or the use of inadequate physics, for example, the use of acoustic simulations when the problem is elastic in nature. Improving the FWI engine to avoid these problems is an area of active research, with global search methods based on Bayesian statistics poised to become more widely used again[105,144–147].

Comparison to other methods. FWI is fundamentally different from classical ray-based tomography[1,2,148] or migration[149,150]. In earthquake seismology, ray-based methods assume that geometrical rays can be traced in (nearly) spherically symmetric or quasi-layered Earth models, and that the effects of additional variations in wave speed can be captured based on first-order perturbation theory. Ray-based methods rely on Fermat's principle, which states that travel-time variations induced by wave-speed perturbations can be calculated by integrating the effects of such wave-speed variations along unperturbed rays, that is, rays in the 1D or 3D background model[90,151]. These ray-based approaches make such tomographic inversions relatively simple and inexpensive, but limits their scope to problems that are, to a large extent, simple in nature. In particular, all classical global tomographic methods — whether involving body waves, surface waves or free oscillation — employ 'crustal corrections' to deal with the effects of Earth's crust on seismic waves[152,153]. Classic seismic depth-migration algorithms include Kirchhoff migration[154], reverse-time migration (RTM)[155], Gaussian beam migration[156], migration by Fourier transform[157] and wave-equation migration[158]. The algorithms require a smooth background wave-speed model, in which an incident wavefield emitted from a seismic source is cross-correlated with a back-propagated wavefield emitted from the receivers, thereby highlighting seismic reflectors. The first-iteration model update in FWI is reminiscent of a migrated image obtained by RTM, except that, in RTM, portions of the wavefield recorded by the receivers are back propagated, whereas in FWI, a measure of the data misfit is back propagated.

In contrast to these classical imaging techniques, FWI requires full 3D numerical simulations based on the seismic-wave equation using 3D Earth models that are iteratively updated as part of the inversion process. As originally conceived, FWI abandons the use of perturbation methods by embracing the full complexity of 3D seismic-wave propagation. As a consequence, FWI can be used to study problems involving strong heterogeneities.

Applications

Applications of seismic FWI can be categorized as controlled-source, earthquake and ambient-noise seismology. In addition to hydrocarbon exploration and deep crustal imaging[40–47], controlled-source applications can be further subdivided by scale into medical imaging[10–14], nondestructive testing[15–24] and near-surface characterization of the top tens of metres of the Earth[25–30], but these are beyond the scope of this Technical Review. Since 2010, ambient-noise FWI based on seismic interferometry[159–161] has emerged[55,56]. In this approach, seismic noise — that is, seismic recordings in the absence of earthquakes — is converted into useful information by cross-correlating noise recorded by pairs of stations, which effectively yields the Green's function between the two receivers. Here, three examples of FWI are highlighted, including frequency-domain visco-acoustic FWI using North Sea data from the Valhall hydrocarbon field, teleseismic FWI of data recorded by the MAUPASACQ array in the western Pyrenees and global FWI using earthquake data from the GSN and regional arrays.

Exploration seismology. To date, FWI has had the biggest impact in exploration seismology, with its use increasing since the successful 2007 blind test inversion[39] (FIG. 1). One application of FWI was in the Valhall field, a large, North Sea hydrocarbon reservoir located in 70-m deepwater[162,163] that was difficult to image with classical methods, owing to a gas cloud in the overburden (as seen as blurred images in the left column of FIG. 3). To better image this reservoir, wide-azimuth ocean-bottom cable data were used for multi-parameter 3D visco-acoustic FWI in the frequency domain[130,131], employing several discrete frequencies in the 3.5–10-Hz range[130,164]. The visco-acoustic model parameterization included the vertical compressional wave speed in the vertical transverse isotropy (VTI) approximation, density and the quality

Banana-doughnut kernels
A finite-frequency version of an infinite-frequency seismic ray, which, in a spherical Earth model, looks like a banana in the vertical plane between the source and receiver and like a doughnut in a cross section perpendicular to this plane.

factor Q, which captures wave attenuation, thus modelling the data using an anisotropic viscous fluid[165]. The resulting inversion images (right column in FIG. 3) clearly identified the gas cloud, as well as channel deposits and scrapes on the paleo-seafloor left by drifting icebergs. At shallow depths, the density model matches well-log data and, furthermore, regions of high attenuation correlated with low-wave-speed zones associated with soft sediments and gas cloud. Thus, incorporating attenuation has only minor effects on the resulting wave-speed model[166] and still allows for imaging through the gas cloud.

Despite the successes of FWI in both onshore and offshore exploration seismology, challenges remain in the construction of a suitable starting model and the acquisition of sufficiently low-frequency data. Additionally, multi-parameter inversions, such as the example here, are difficult, owing to inherent trade-offs between model parameters[139,167,168].

Teleseismic FWI. Another application of FWI uses teleseismic waves, which are generated by distant earthquakes, to image areas such as subduction zones or mountain belts. In this application, the teleseismic wavefield entering the region of interest is approximated by a simplified incoming wave, which gives rise to a more complex wavefield in the smaller domain of

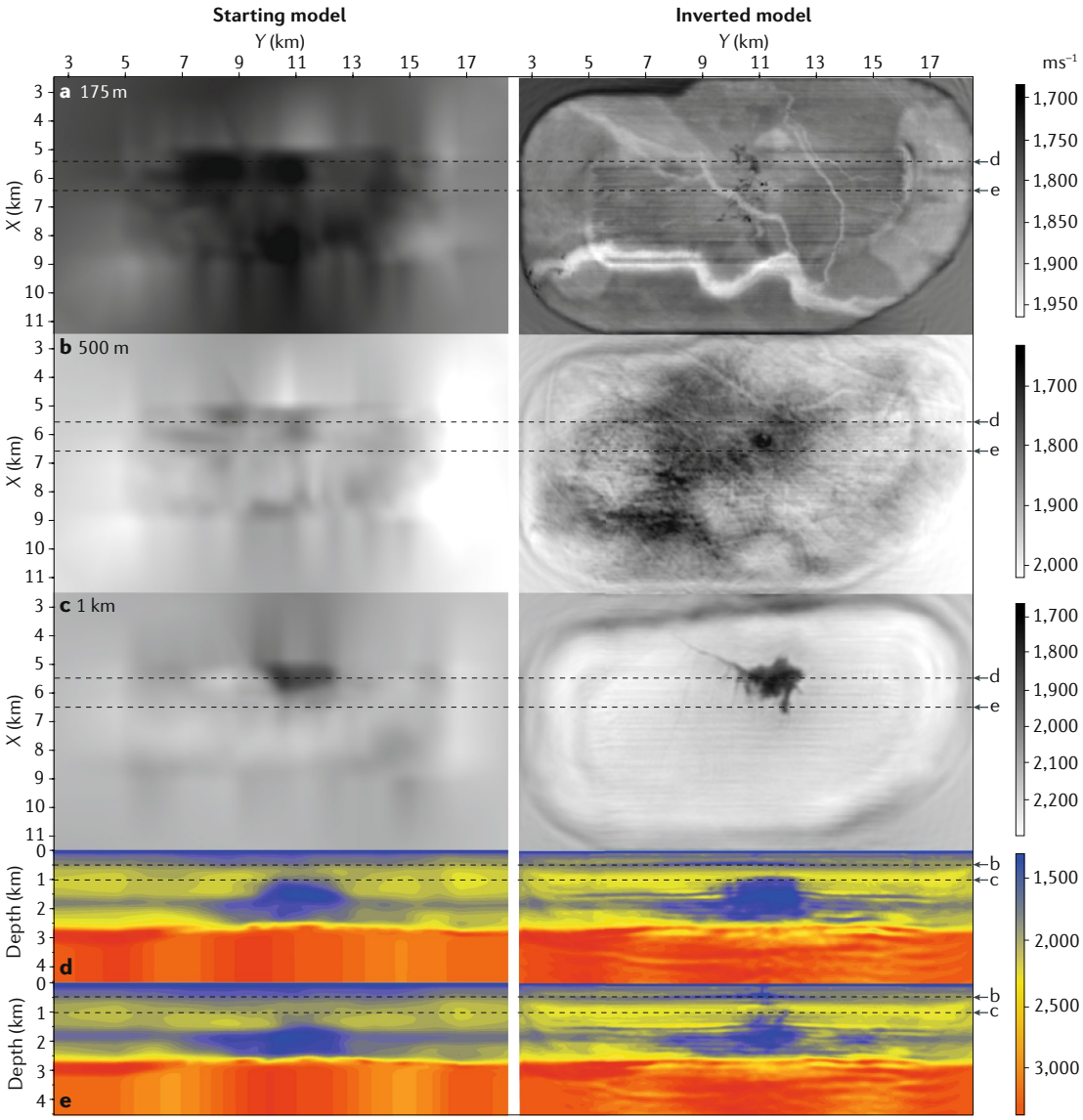

Fig. 3 | **Multi-parameter visco-acoustic FWI of the Valhall oil field.** Slices of the starting model (vertical wave speed) built by reflection travel-time tomography (courtesy of BP) are shown in the left column, with the corresponding inverted model in the right column. The horizontal slices at depths of 175 m (part **a**), 500 m (part **b**) and 1 km (part **c**) across the gas cloud. The inline vertical slices pass through the gas cloud (X = 5.6 km, part **d**) and near its periphery (X = 6.25 km, part **e**). In the right panel of part **a**, channel deposits can be seen at a depth of 175 m. Moreover, a diffractor generated by the platform can be seen around X = 6 km and Y = 11 km. In the 500-m-depth slice, the linear structures correspond to scrapes on the paleo-seafloor left by drifting icebergs. The 1-km-depth slice is across the gas cloud with fractures. The signature of one of these fractures is seen in the vertical sections. FWI, full-waveform inversion. Left panels of parts **a**–**e** adapted with permission from REF.[130], Oxford University Press. Right panels of parts **a**–**e** adapted with permission from REF.[131], Oxford University Press.

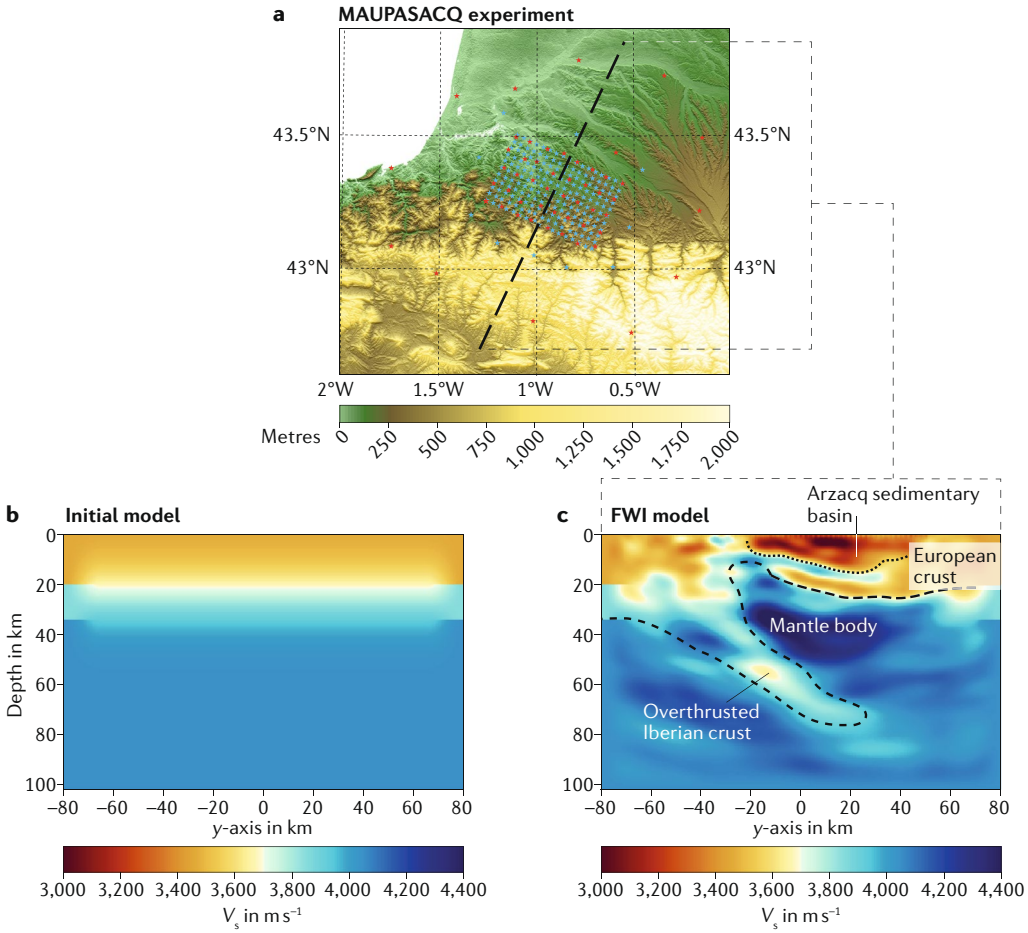

Fig. 4 | **Teleseismic FWI experiment using the MAUPASACQ array in the western Pyrenees. a** | Geographical location and array layout. The red and blue stars label broadband and short-period stations, respectively. **b** | SW–NE cross section of the starting model. The shear wave speed V_s in m s^{-1}. **c** | SW–NE cross section of the inverted shear wave speed model. FWI, full-waveform inversion. Images courtesy of S. Beller (Princeton University, USA) and S. Chevrot (Université de Toulouse III Paul Sabatier, France).

interest[169–174]. In this way, the teleseismic wave can be modelled with simple classical techniques, whereas the complex local wavefield is modelled based on full 3D seismic-wave-equation solvers, and FWI is performed only within the region of interest. This is substantially cheaper computationally while still allowing for the structural and compositional resolution enabled by FWI.

Teleseismic FWI[175–177] was used on the MAUPASACQ data set of the OROGEN project (FIG. 4), in which ten teleseismic earthquakes were recorded by nearly 450 broadband and short-period stations in the Pyrenees[178,179]. After six iterations using three-component seismographic data with a shortest period of 3 s, this model clearly showed the overthrusted Iberian crust and the shallow low-wave-speed Arzacq sedimentary basin. Although teleseismic FWI has given new insight into the structure of Earth's crust, there remain challenges in its implementation. The main difficulty is when the assumption that the incoming teleseismic wavefield is relatively simple is no longer valid. In this case, the structure outside the domain of interest can contaminate the inversion results, leading to a poorly resolved model.

Earthquake seismology. The final application discussed here illustrates FWI in earthquake seismology, which was first used on regional and continental scales[48–52], namely southern California and Australasia. Continental-scale imaging of Europe[91,180–187] was spearheaded by the QUEST Initial Training Network in computational seismology, started in 2009. Subsequent studies focused on the construction of FWI-based models of North America[188,189], Asia[190–192] and Antarctica[193].

After these large-scale successes, imaging of the crust and mantle of a global scale was performed using a hybrid approach that combined 3D forward simulations[194] with inverse simulations based on the NACT developed by Li and Romanowicz[195], resulting in remarkable images of numerous mantle plumes[53,196]. However, it has been reported that hybrid methods may be more error-prone than classical approximate methods[197]. Simultaneously, the multiscale Collaborative Seismic Earth Model was being pursued[198–200]. The first application of global FWI, GLAD-M15, was a transversely isotropic mantle model based on seismograms from 253 earthquakes with periods greater than 17 s and involved 15 quasi-Newton iterations on a Cray XK7 supercomputer named 'Titan'[54].

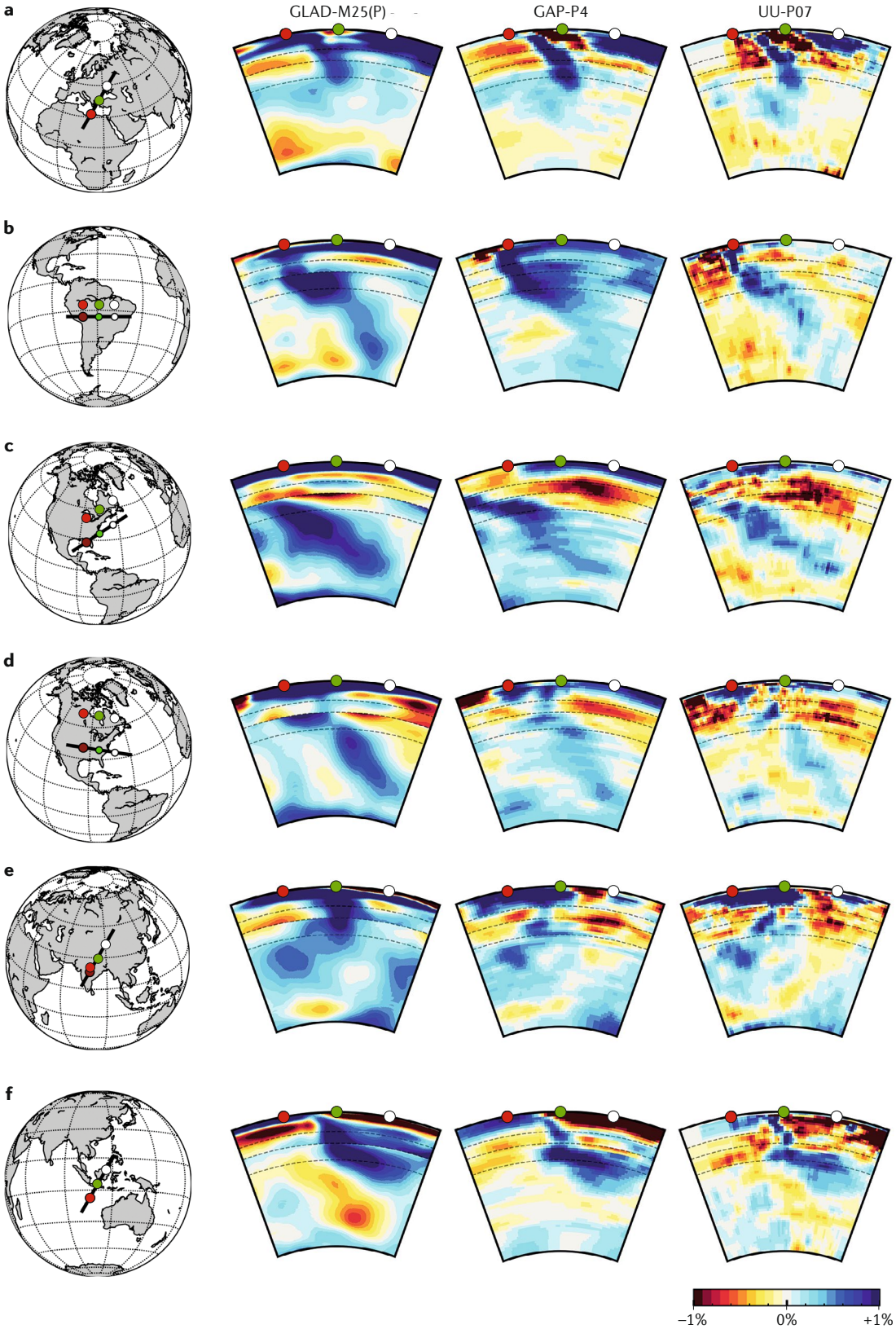

Fig. 5 | **Vertical cross sections of compressional wave-speed perturbations in various subduction zones.** The same subduction zone is shown for each of three models: GLAD-M25 (compressional wave speed; left column), GAP-P4 (REF.[201]) (middle column) and UU-P07 (REF.[202]) (right column). The map on the far-left corner of each row shows the cross section with colour-coded red, green and white dots for geographical reference along the sections. The dashed-black semicircles in the cross sections denote depths of 410 km, 660 km and 1,000 km. **a** | Hatteras. **b** | Wichita. **c** | Aegean. **d** | South America. **e** | Nepal. **f** | Sunda. Images courtesy of W. Lei (Princeton University, USA).

In 2019, GLAD-M15 was updated to GLAD-M25, using an earthquake database of 1,480 events and involving ten quasi-Newton tomographic iterations (unpublished observations, J.T.). Subduction zones from this model (FIG. 5) reveal many features of the subsurface that were unresolved in P models, such as GAP-P4 (REF.[201]) and UU-P07 (REF.[202]). For example, for the cuts across the ancient Farallon slab (FIG. 5a,b), which penetrates deeply into the lower mantle[5,6,203], the slab is only weakly expressed below 1,000 km in the two P models but is clearly seen in the GLAD-M25 model. The difference can be attributed to the use of finite-frequency Fréchet derivatives in FWI, as well as increased data coverage from the USArray. In other cases, the GLAD-M25 results confirmed the structures observed in other models, such as the penetration of the slab deep into the lower mantle in the Aegean subduction zone (FIG. 5c), the ponding and then sinking of the South American slab to the CMB (FIG. 5d), the two fast anomalies below the Himalayas (FIG. 5e) and the flattening and spreading of the subducting plate below the Sunda Arc[204] (FIG. 5f). This flattening was explained as the subducted slab thickening and buckling to form a dense megalith above the discontinuity at 660 km before sinking into the lower mantle[204]. What the current generation of global FWI models[53,54] has in common is that the level of heterogeneity is significantly larger than in models based on classical methods.

In the second global-scale FWI example, the 3D morphology of the African superplume is illustrated based on the GLAD-M25 FWI model (FIG. 6). The model shows a mantle plume rising from the CMB with a broad base tilting northward and a thinning neck in the upper mantle before it reaches the phase boundary at 660 km and flattens, and then develops into two subplumes (Afar and East Lake Victoria), which supply the East African Rift. Although the existence of the two superplumes underneath Africa and the Pacific has been known for decades[4,205], this more detailed image of the African plume shows strong perturbations in shear wave speed (>2%) all the way from the CMB to the surface, with implications for the associated thermochemistry. These perturbations are too large to be purely thermal in nature and must include a compositional contribution.

Even with the substantial advances in the applications of earthquake-seismology-based FWI and the resulting understanding of the deep Earth, the highly uneven distribution of earthquakes and seismographic stations remains a major challenge to its use. With earthquakes confined primarily to plate boundaries and seismic instruments predominantly located in the Northern Hemisphere and on the continents, the most accurate implementations of FWI are in Northern Hemisphere continental settings, whereas southern hemispheric and marine settings remain underimaged. Balancing this uneven distribution of sources and receivers in the FWI process by suitable weighting is, therefore, important[195,206].

Opportunities and challenges

FWI for Earth imaging has evolved and surmounted many technical and practical hurdles since its conception in 1977, but aspects of its implementation are still problematic. Here, some of the challenges and opportunities for FWI applications in the geosciences are summarized, including multi-parameter optimization, computational efficiency, uncertainty quantification, source encoding and global search methodology.

Multi-parameter inversions. Early applications of FWI focused on the single-parameter determination of 2D and 3D sound-speed images, but, today, multi-parameter FWI is common, as exemplified in the global GLAD-M25 model (FIGS 5,6) and by the visco-acoustic VTI model[131] (FIG. 3). Acoustic VTI parameterization is commonly used in exploration seismology to explain the observed directional dependence of P waves[207–209], whereas an elastic VTI parameterization is used to explain wave-speed differences between horizontally and vertically polarized shear waves in global and regional seismology. Global surface waves exhibit azimuthal anisotropy in the form of a directional dependence of the Love-wave and Rayleigh-wave phase speeds[210,211], and regional FWI was used to identify such anisotropy — called horizontal transverse isotropy in industry — in the European asthenosphere and lower crust[182]. Inversions for more general anisotropy, at a minimum tilted transverse isotropy — that is, transverse isotropy with a tilted symmetry axis — should become feasible[212–214]. Beyond these examples, there is opportunity for further development of this technique, as joint inversions of seismic wave speeds and attenuation can be performed because higher frequencies attenuate faster than lower frequencies during seismic-wave propagation. Such inversions are being researched in both exploration and global seismology[131,166,183,215–218], fulfilling a strategy envisioned in 1988 (REF.[97]). Additionally, acoustic FWI workflows, which are commonly used in industrial applications, should be updated to (an)elastic FWI workflows, which is the standard in earthquake seismology.

In earthquake seismology, the most difficult seismic parameter to constrain is often the mass density[219,220], because global seismic observables are generally insensitive to this parameter. Indirect density sensitivity can be measured in exploration seismology as, here, the commonly used reflected waves are sensitive to contrasts in impedance (the product of density and wave speed). In this context, it may be a good strategy to try to determine the optimal observables for constraining a specific parameter, such as the density[221].

Computational efficiency. The FWI workflow (FIG. 2) is complex and prone to human errors and hardware failures, and automated recovery mechanisms are required at scale[189,222–224]. Although 2D FWI can be carried out on a workstation or even a single graphics processing unit, the computational requirements for 3D (an)elastic FWI remain substantial because of the amount of data that needs to be analysed and the full 3D simulations of seismic-wave propagation that are required to calculate the synthetic seismograms and Fréchet derivatives of a misfit function. Ensuring that software scales and takes advantage of the latest hardware advances, such as in graphics processing unit or quantum computing, requires continual investment in software development. Version control (to ensure stability and reproducibility),

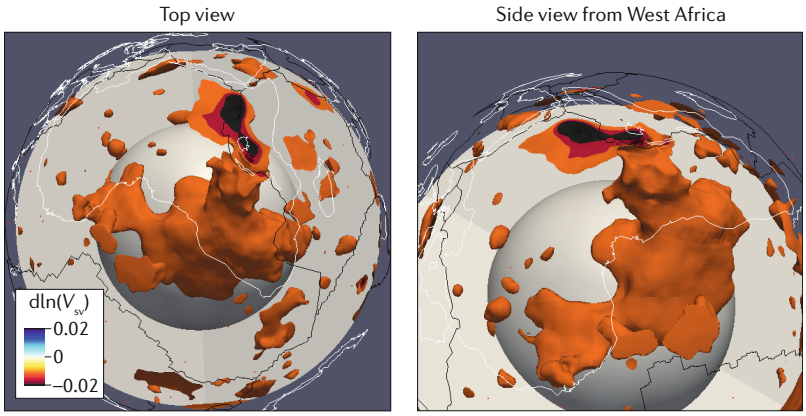

Fig. 6 | **3D morphology of the African superplume from two angles.** The superplume was revealed by the −1.1% isosurface of vertically polarized shear wave-speed perturbations in the global GLAD-M25 model at depths between the core–mantle boundary and 350 km. dln(V_{SV}) denotes a logarithmic perturbation in shear wave-speed. Images courtesy of Y. Ruan (Nanjing University, China) and W. Lei (Princeton University, USA).

automated testing (to detect code failures quickly) and code documentation are paramount.

A key challenge in FWI is the data volumes involved, which frequently involves terabytes of earthquake data and petabytes of offshore exploration data, making data assimilation challenging and necessitating I/O management[127,225,226]. To effectively manage I/O in global FWI, a new data format — the Adaptable Seismic Data Format[227] — was created. There is the additional issue that the large volume of poor-quality earthquake data must be culled from the source database in a robust, automated fashion[228]. For this, data analytics and machine learning in FWI could be used to identify good-quality measurements for assimilation[229].

Finally, data and model visualization are crucial for data mining and feature extraction, as illustrated by the identification of scrapes of drifting icebergs left on the paleo-seafloor (FIG. 3) and the assessment of the morphology of the African superplume (FIG. 6). The sheer volume of model data can make this visual process of scientific discovery slow and cumbersome.

Uncertainty quantification. Once a model has been determined, it is important to assess its robustness; that is, which features are well resolved. This 'uncertainty quantification' remains a challenge in FWI[230] because traditional checkboard tests are too computationally expensive and 'point-spread function' tests[231,232], which assess the resolution and trade-off between model parameters, are limited, targeting just one specific location of interest. Ideally, the currently used quasi-Newton methods would be abandoned in favour of Bayesian inference[105,233], which provides the complete, possibly multi-modal, a posteriori model distribution, but for this to happen, the computational cost of FWI would have to be reduced dramatically. Meanwhile, there have been successful attempts at sampling the a posteriori model distribution in the vicinity of the global minimum based on random probing[234,235], Kalman filtering[236,237] and the square-root variable-metric method[238,239]. Synthetic examples of these techniques have focused on the Marmousi model[240], as well as a real data set from the Valhall oil field[236].

Source encoding. Although frequency-domain wave-propagation solvers have the benefit in that they are independent of the number of sources[37,241], time-domain solvers scale linearly with the number of sources. In exploration seismology, this issue has been dealt with using source encoding[242–248], which combines data from different sources in one encoded 'supergather', thereby dramatically reducing the computational cost. The challenge had been that the encoded contributions from distinct sources are difficult to completely unravel, leading to 'crosstalk'[249], which contaminates the Fréchet derivatives and, ultimately, the model. This results in either convergence never being reached or converging on the wrong model. Recently, several successful methods of crosstalk-free source encoding have been developed[250–254]. For example, in one method[253,254], the encoded forward and adjoint wave fields are run until they reach steady state, at which point they are 'decoded' to obtain their stationary parts, based on an integration over a time interval that is the reciprocal of the encoded frequency spacing. These parts are then combined for all sources to obtain crosstalk-free Fréchet derivatives, thus enabling convergence on the optimal model.

Global search methods. As discussed previously, current FWI algorithms often invoke quasi-Newton local optimization methods, which are prone to getting 'stuck' in local minima of the misfit function. But as FWI becomes faster owing to advances in computing and more intelligent algorithms, for example, source encoding or sparsity promotion and compressive sensing[255–259], the possibility of stochastic inversion using Bayesian techniques[144–146] becomes enticing. Global search methods based on Bayes' theorem[105] provide an entire posterior model distribution, overcoming issues associated with the single 'optimal' models currently used. The problem is that these solutions require sampling of the entire model space to determine the posterior, which, in FWI, is often prohibitively computationally expensive.

In Bayesian inference, the Markov chain Monte Carlo (MCMC) technique may be used to sample the posterior distribution, for example, based on the Metropolis–Hastings algorithm[260–262]. Unfortunately, optimization algorithms — MCMC algorithms included — are doomed by 'no-free-lunch' theorems[263,264], which state that all algorithms are computationally equal and that only the injection of prior knowledge can break the impasse. A further sampling challenge is due to the 'curse of dimensionality', by which the volume of the data space increases exponentially as the number of model dimensions grows[265,266]. In this context, the Hamiltonian Monte Carlo method[267] is an MCMC technique that uses derivatives of the probability density function to more efficiently sample the posterior[268,269]. Thus, whereas MCMC requires just evaluations of the misfit, Hamiltonian Monte Carlo also requires the misfit gradient, which may be accomplished based on the adjoint-state method used in the FWI workflow presented here. Promising first applications in

Checkboard tests
Inversion experiments in which synthetic data are generated for a checkboard model parameter pattern. These data are then inverted to assess how well the checkboard pattern can be recovered.

Marmousi model
A fictitious model created by a consortium led by the Institut Français du Pétrole. The initial model was 2D acoustic but there is an elastic version called Marmousi2.

tomography[147] and uncertainty quantification[270] were recently presented.

Conclusions and perspective

The idea of seismic FWI was conceived more than 35 years ago and, today, is used in many disciplines of science, engineering and medicine, spanning nine orders of magnitude in frequency and wavelength. Performing FWI at scale continues to be a nontrivial exercise, requiring abundant, high-quality data, access to large computational resources and a multidisciplinary research team that comprises seismologists, computational scientists and applied mathematicians; moreover, continual investments in algorithmic and software developments are paramount. Despite considerable computational costs, algorithmic complexities and workflow-management challenges, FWI is more than worthwhile for what it offers in terms of model resolution and accuracy. In industry, these advantages translate into substantial income for petroleum companies, for example, by opening up hydrocarbon fields that were previously thought to be unimageable and, therefore, unexploitable. In earthquake seismology, the use of adjoint-based FWI methods offer the promise of higher resolution, such as in the form of sharper, more intense images of subduction zones and mantle plumes, thereby opening up new avenues for geophysical and geochemical interpretations. For all applications, crosstalk-free source encoding, Bayesian inference accelerated by Hamiltonian Monte Carlo techniques, and machine learning and data analytics will likely have a marked impact on FWI, enhancing our ability to image Earth's subsurface.

Published online 9 December 2019

1. Aki, K., Christoffersson, A. & Husebye, E. S. Determination of the three-dimensional seismic structure of the lithosphere. *J. Geophys. Res.* **82**, 277–296 (1977).
2. Dziewoński, A. M., Hager, B. H. & O'Connell, R. J. Large-scale heterogeneities in the lower mantle. *J. Geophys. Res.* **82**, 239–255 (1977).
3. Woodhouse, J. H. & Dziewoński, A. M. Mapping the upper mantle: three-dimensional modeling of Earth structure by inversion of seismic waveforms. *J. Geophys. Res.* **89**, 5953–5986 (1984). **The first application of global waveform tomography in earthquake seismology using mantle waves**.
4. Masters, T. G., Johnson, S., Laske, G. & Bolton, H. A shear-velocity model of the mantle. *Phil. Trans. R. Soc. Lond. A* **354**, 1385–1411 (1996).
5. Van der Hilst, R. D., Widiyantoro, S. & Engdahl, R. Evidence for deep mantle circulation from global tomography. *Nature* **386**, 578–584 (1997).
6. Grand, S. P., Van der Hilst, R. D. & Widiyantoro, S. High resolution global tomography: a snapshot of convection in the Earth. *Geol. Soc. Am. Today* **7** (1997).
7. Bassin, C., Laske, G. & Masters, G. The current limits of resolution for surface wave tomography in North America. *EOS Trans. AGU* **81** (2000).
8. Laske, G., Masters, G., Ma, Z. & Pasyanos, M. Update on CRUST1.0 – A 1-degree global model of Earth's crust. *Geophys. Res. Abstr.* **15**, 2658 (2013).
9. Ratcliff, D. W., Gray, S. H. & Whitmore, N. D. Jr. Seismic imaging of salt structures in the Gulf of Mexico. *Lead. Edge* **11**, 15–31 (1992).
10. Schreiman, J., Gisvold, J., Greenleaf, J. F. & Bahn, R. Ultrasound transmission computed tomography of the breast. *Radiology* **150**, 523–530 (1984).
11. Duric, N. et al. in *Proc. Medical Imaging 2015: Ultrasonic Imaging and Tomography* Vol. 9419 (International Society for Optics and Photonics, 2015).
12. Li, C., Sandhu, G. Y., Boone, M. & Duric, N. in *Proc. Medical Imaging 2017: Ultrasonic Imaging and Tomography* Vol. 10139 (International Society for Optics and Photonics, 2017).
13. Boehm, C., Martiartu, N. K., Vinard, N., Balic, I. J. & Fichtner, A. in *Proc. Medical Imaging 2018: Ultrasonic Imaging and Tomography* Vol. 10580 (International Society for Optics and Photonics, 2017).
14. Wiskin, J. et al. Full wave 3D inverse scattering: 21st century technology for whole body imaging. *J. Acoust. Soc. Am.* **145**, 1857–1857 (2019).
15. Huthwaite, P. & Simonetti, F. High-resolution guided wave tomography. *Wave Motion* **50**, 979–993 (2013).
16. Huthwaite, P. Guided wave tomography with an improved scattering model. *Proc. R. Soc. A* **472**, 20160643 (2016).
17. Rao, J., Ratassepp, M. & Fan, Z. Guided wave tomography based on full waveform inversion. *IEEE Trans. Ultrason. Ferroelectr. Freq. Control* **63**, 737–745 (2016).
18. Seidl, R. & Rank, E. Iterative time reversal based flaw identification. *Comput. Math. Appl.* **72**, 879–892 (2016).
19. Rao, J., Ratassepp, M. & Fan, Z. Limited-view ultrasonic guided wave tomography using an adaptive regularization method. *J. Appl. Phys.* **120**, 194902 (2016).
20. Jalinoos, F., Tran, K. T., Nguyen, T. D. & Agrawal, A. K. Evaluation of bridge abutments and bounded wall type structures with ultraseismic waveform tomography. *J. Bridge Eng.* **22**, 04017104 (2017).
21. Rao, J., Ratassepp, M. & Fan, Z. Investigation of the reconstruction accuracy of guided wave tomography using full waveform inversion. *J. Sound Vib.* **400**, 317–328 (2017).
22. Lamert, A., Nguyen, L. T., Friederich, W. & Nestorović, T. Imaging disturbance zones ahead of a tunnel by elastic full-waveform inversion: adjoint gradient based inversion vs. parameter space reduction using a level-set method. *Undergr. Space* **3**, 21–33 (2018).
23. Nguyen, L. T. & Modrak, R. T. Ultrasonic wavefield inversion and migration in complex heterogeneous structures: 2D numerical imaging and nondestructive testing experiments. *Ultrasonics* **82**, 357–370 (2018).
24. He, J., Rocha, D. C., Leser, P. E., Sava, P. & Leser, W. P. Least-squares reverse time migration (LSRTM) for damage imaging using Lamb waves. *Smart Mater. Struct.* **28**, 065010 (2019).
25. Gao, F., Levander, A. R., Pratt, R. G., Zelt, C. A. & Fradelizio, G. L. Waveform tomography at a groundwater contamination site: VSP-surface data set. *Geophysics* **71**, H1–H11 (2006).
26. Chen, J., Zelt, C. A. & Jaiswal, P. Detecting a known near-surface target through application of frequency-dependent traveltime tomography and full-waveform inversion to P- and SH-wave seismic refraction data. *Geophysics* **82**, R1–R17 (2017).
27. Alam, M. I. & Jaiswal, P. Near surface characterization using VP/VS and Poisson's ratio from seismic refractions. *J. Environ. Eng. Geophysics* **22**, 101–109 (2017).
28. Alam, M. I. Near-surface characterization using traveltime and full-waveform inversion with vertical and horizontal component seismic data. *Interpretation* **7**, T141–T154 (2019).
29. Wang, Y. et al. Tunnel detection at Yuma Proving Ground, Arizona, USA – Part 1: 2D full-waveform inversion experiment. *Geophysics* **84**, B95–B105 (2019).
30. Smith, J. A. et al. Tunnel detection at Yuma Proving Ground, Arizona, USA – Part 2: 3D full-waveform inversion experiments. *Geophysics* **84**, B107–B120 (2019).
31. Gauthier, O., Virieux, J. & Tarantola, A. Two-dimensional non-linear inversion of seismic waveforms: numerical results. *Geophysics* **51**, 1387–1403 (1986).
32. Mora, P. Nonlinear two-dimensional elastic inversion of multi-offset seismic data. *Geophysics* **52**, 1211–1228 (1987).
33. Mora, P. Elastic wavefield inversion of reflection and transmission data. *Geophysics* **53**, 750–759 (1987).
34. Pratt, R. G. & Worthington, M. H. Inverse theory applied to multi-source cross-hole tomography. Part 1: Acoustic wave-equation method. *Geophys. Prospecting* **38**, 287–310 (1990). **Successful application of frequency-domain waveform inversion using crosshole transmitted waves**.
35. Igel, H., Djikpréssé, H. & Tarantola, A. Waveform inversion of marine reflection seismograms for *P* impedance and Poisson's ratio. *Geophys. J. Int.* **124**, 363–371 (1996).
36. Pratt, R. G., Song, Z. M., Williamson, P. R. & Warner, M. Two-dimensional velocity models from wide-angle seismic data by wavefield inversion. *Geophys. J. Int.* **124**, 323–340 (1996).
37. Pratt, R. G. Seismic waveform inversion in the frequency domain, Part 1: Theory and verification in a physical scale model. *Geophysics* **64**, 888–901 (1999).
38. Pratt, R. G. & Shipp, R. M. Seismic waveform inversion in the frequency domain, Part 2: Fault delineation in sediments using crosshole data. *Geophysics* **64**, 902–914 (1999).
39. Brenders, A. J. & Pratt, G. Full waveform tomography for lithospheric imaging: results from a blind test in a realistic crustal model. *Geophys. J. Int.* **168**, 133–151 (2007). **Successful blind test inversion based on seismic waveform inversion in exploration seismology**.
40. Dessa, J.-X. et al. Multiscale seismic imaging of the eastern Nankai trough by full waveform inversion. *Geophys. Res. Lett.* **31** (2004).
41. Ravaut, C. et al. Multiscale imaging of complex structures from multifold wide-aperture seismic data by frequency-domain full-waveform tomography: Application to a thrust belt. *Geophys. J. Int.* **159**, 1032–1056 (2004).
42. Operto, S., Virieux, J., Dessa, J.-X. & Pascal, G. Crustal seismic imaging from multifold ocean bottom seismometer data by frequency domain full waveform tomography: Application to the eastern Nankai trough. *J. Geophys. Res. Solid Earth* **111** (2006).
43. Kamei, R., Pratt, R. G. & Tsuji, T. Waveform tomography imaging of a megasplay fault system in the seismogenic Nankai subduction zone. *Earth Planet. Sci. Lett.* **317–318**, 343–353 (2012).
44. Jian, H., Singh, S. C., Chen, Y. J. & Li, J. Evidence of an axial magma chamber beneath the ultraslow-spreading Southwest Indian Ridge. *Geology* **45**, 143–146 (2017).
45. Górszczyk, A., Operto, S. & Malinowski, M. Toward a robust workflow for deep crustal imaging by FWI of OBS data: The eastern Nankai Trough revisited. *J. Geophys. Res. Solid Earth* **122**, 4601–4630 (2017).
46. Huot, G. & Singh, S. C. Seismic evidence for fluid/gas beneath the Mentawai Fore-Arc Basin, Central Sumatra. *J. Geophys. Res. Solid Earth* **123**, 957–976 (2018).
47. Gorszczyk, A., Operto, S., Schenini, L. & Yamada, Y. Crustal-scale depth imaging via joint full-waveform inversion of ocean-bottom seismometer data and pre-stack depth migration of multichannel seismic data: a case study from the eastern Nankai Trough. *Solid Earth* **10**, 765–784 (2019).
48. Chen, P., Zhao, L. & Jordan, T. H. Full 3D tomography for the crustal structure of the Los Angeles region. *Bull. Seism. Soc. Am.* **97**, 1094–1120 (2007). **Earthquake seismology FWI of the Los Angeles region**.

49. Tape, C., Liu, Q., Maggi, A. & Tromp, J. Adjoint tomography of the southern California crust. *Science* **325**, 988–992 (2009).
Earthquake seismology FWI of the southern California crust.
50. Tape, C., Liu, Q., Maggi, A. & Tromp, J. Seismic tomography of the southern California crust based on spectral-element and adjoint methods. *Geophys. J. Int.* **180**, 433–462 (2010).
51. Fichtner, A., Kennett, B. L. N., Igel, H. & Bunge, H. P. Full seismic waveform tomography for upper-mantle structure in the Australasian region using adjoint methods. *Geophys. J. Int.* **179**, 1703–1725 (2009).
52. Fichtner, A., Kennett, B. L. N., Igel, H. & Bunge, H.-P. Full waveform tomography for radially anisotropic structure: New insights into present and past states of the Australasian upper mantle. *Earth Planet. Sci. Lett.* **290**, 270–280 (2010).
53. French, S. W. & Romanowicz, B. Broad plumes rooted at the base of the Earth's mantle beneath major hotspots. *Nature* **525**, 95–99 (2015).
The first application of global waveform inversion based on a hybrid method, combining forward simulations in 3D models with inverse simulations based on a perturbation method.
54. Bozdağ, E. et al. Global adjoint tomography: first-generation model. *Geophys. J. Int.* **207**, 1739–1766 (2016).
The first application of global FWI.
55. Tromp, J., Luo, Y., Hanasoge, S. & Peter, D. Noise cross-correlation sensitivity kernels. *Geophys. J. Int.* **183**, 791–819 (2010).
56. Sager, K., Ermert, L., Boehm, C. & Fichtner, A. Towards full waveform ambient noise inversion. *Geophys. J. Int.* **212**, 566–590 (2018).
57. Virieux, J. & Operto, S. An overview of full-waveform inversion in exploration geophysics. *Geophysics* **74**, WCC1–WCC26 (2009).
58. Fichtner, A. *Full Seismic Waveform Modelling and Inversion* (Springer, 2010).
59. Liu, Q. & Gu, Y. Seismic imaging: from classical to adjoint tomography. *Tectonophysics* **566–567**, 31–66 (2012).
60. Bamberger, A., Chavent, G. & Lailly, P. Une application de la théorie du contrôle à un problème inverse de sismique. *Ann. Geophys.* **33**, 183–200 (1977).
61. Lailly, P. in *Conf. on Inverse Scattering: Theory and Application* (ed Bednar, J.) 206–220 (Society for Industrial and Applied Mathematics, 1983).
62. Tarantola, A. Inversion of seismic reflection data in the acoustic approximation. *Geophysics* **49**, 1259–1266 (1984).
The magnificent work at the root of FWI.
63. Lions, J. L. & Magenes, E. *Non-Homogeneous Boundary Value Problems and Applications* (Springer, 1972).
64. Chavent, G. in *Identification of Parameter Distributed Systems* (eds Goodson, R. E. & Polis, M. P.) 65–74 (American Society of Mechanical Engineers, 1974).
65. Le Dimet, F.-X. & Talagrand, O. Variational algorithms for analysis and assimilation of meteorological observations: theoretical aspects. *Tellus A* **38**, 97–110 (1986).
66. Talagrand, O. & Courtier, P. Variational assimilation of meteorological observations with the adjoint vorticity equation. I: Theory. *Q. J. R. Meteorol. Soc.* **113**, 1311–1328 (1987).
67. Nolet, G. in *Seismic Tomography* (ed. Nolet, G.) 301–322 (D. Reidel, 1987).
68. Nolet, G. Partitioned waveform inversion and two-dimensional structure under the Network of Autonomously Recording Seismograph. *J. Geophys. Res.* **95**, 8499–8512 (1990).
Introduction of partitioned waveform inversion in earthquake seismology.
69. Zielhuis, A. & Nolet, G. Deep seismic expression of an ancient plate boundary in Europe. *Science* **265**, 79–81 (1994).
70. Li, X. D. & Tanimoto, T. Waveforms of long-period body waves in a slightly aspherical Earth model. *Geophys. J. Int.* **112**, 92–102 (1993).
71. Li, X. D. & Romanowicz, B. Comparison of global waveform inversions with and without considering cross-branch modal coupling. *Geophys. J. Int.* **121**, 695–709 (1995).
72. Li, X.-D. & Romanowicz, B. Global mantle shear velocity model developed using nonlinear asymptotic coupling theory. *J. Geophys. Res.* **101**, 22245–22272 (1996).
Construction of a global shear wave speed model based on NACT.
73. Marquering, H., Dahlen, F. A. & Nolet, G. Three-dimensional sensitivity kernels for finite-frequency traveltimes: the banana-doughnut paradox. *Geophys. J. Int.* **137**, 805–815 (1999).
Introduction of finite-frequency sensitivity kernels, affectionately known as 'banana-doughnut' kernels.
74. Dahlen, F. A., Hung, S.-H. & Nolet, G. Fréchet kernels for finite-frequency traveltimes - I. Theory. *Geophys. J. Int.* **141**, 157–174 (2000).
75. Dahlen, F. A. & Baig, A. M. Fréchet kernels for body-wave amplitudes. *Geophys. J. Int.* **150**, 440–466 (2002).
76. Montelli, R., Nolet, G., Dahlen, F. A. & Masters, G. A catalogue of deep mantle plumes: new results from finite-frequency tomography. *Geochem. Geophys. Geosyst.* **7**, Q11007 (2006).
77. Tromp, J., Tape, C. & Liu, Q. Y. Seismic tomography, adjoint methods, time reversal and banana-doughnut kernels. *Geophys. J. Int.* **160**, 195–216 (2005).
This article draws connections between finite-frequency sensitivity kernels, adjoint-state methods and time-reversal imaging.
78. Tape, C., Liu, Q. & Tromp, J. Finite-frequency tomography using adjoint methods — methodology and examples using membrane surface waves. *Geophys. J. Int.* **168**, 1105–1129 (2007).
79. Liu, Q. & Tromp, J. Finite-frequency kernels based on adjoint methods. *Bull. Seism. Soc. Am.* **96**, 2383–2397 (2006).
80. Liu, Q. & Tromp, J. Finite-frequency sensitivity kernels for global seismic wave propagation based upon adjoint methods. *Geophys. J. Int.* **174**, 265–286 (2008).
81. Plessix, R. E. A review of the adjoint-state method for computing the gradient of a functional with geophysical applications. *Geophys. J. Int.* **167**, 495–503 (2006).
82. Nocedal, J. & Wright, S. *Numerical Optimization* 2nd edn (Springer, 2006).
83. Biegler, L., Ghattas, O., Heinkenschloss, M. & van Bloemen Waanders, B. in *Large-Scale PDE-Constrained Optimization* Vol. 30 (eds Biegler, L. T., Heinkenschloss, M., Ghattas, O. & van Bloemen Waanders, B.) 3–13 (Springer, 2003).
84. Dziewoński, A. & Anderson, D. Preliminary reference Earth model. *Phys. Earth Planet. Inter.* **25**, 297–356 (1981).
85. Ritzwoller, M. H. & Lavely, E. M. Three-dimensional models of the Earth's mantle. *Rev. Geophys.* **33**, 1–66 (1995).
86. Trampert, J. & Woodhouse, J. H. Assessment of global phase velocity models. *Geophys. J. Int.* **144**, 165–174 (2001).
87. Becker, T. W. & Boschi, L. A comparison of tomographic and geodynamic mantle models. *Geochem. Geophys. Geosyst* **3**, 1003 (2002).
88. Lekic, V., Cottaar, S., Dziewonski, A. & Romanowicz, B. Cluster analysis of global lower mantle tomography: a new class of structure and implications for chemical heterogeneity. *Earth Planet. Sci. Lett.* **357–358**, 68–77 (2012).
89. Bunks, C., Saleck, F. M., Zaleski, S. & Chavent, G. Multiscale seismic waveform inversion. *Geophysics* **60**, 1457–1473 (1995).
Introduction of the important concept of multiscale waveform inversion.
90. Dahlen, F. A. & Tromp, J. *Theoretical Global Seismology* (Princeton Univ. Press, 1998).
91. Zhu, H., Bozdağ, E., Peter, D. & Tromp, J. Structure of the European upper mantle revealed by adjoint tomography. *Nat. Geosci.* **5**, 493–498 (2012).
Continental-scale VTI FWI of the European crust and upper mantle.
92. Plessix, R.-E., Baeten, G., de Maag, J. & ten Kroode, F. Full waveform inversion and distance separated simultaneous sweeping: a study with a land seismic data set. *Geophys. Prospecting* **60**, 733–747 (2012).
93. Igel, H. *Computational Seismology* (Oxford Univ. Press, 2016).
94. Virieux, J. *SH*-wave propagation in heterogeneous media: velocity-stress finite-difference method. *Geophysics* **49**, 1933–1942 (1984).
95. Virieux, J. *P-SV* wave propagation in heterogeneous media: velocity-stress finite-difference method. *Geophysics* **51**, 889–901 (1986).
96. Levander, A. R. Fourth-order finite-difference *P-SV* seismograms. *Geophysics* **53**, 1425–1436 (1988).
97. Tarantola, A. Theoretical background for the inversion of seismic waveforms, including elasticity and attenuation. *Pure Appl. Geophys.* **128**, 365–399 (1988).
98. Crase, E., Pica, A., Noble, M., McDonald, J. & Tarantola, A. Robust elastic non-linear waveform inversion: application to real data. *Geophys. J. Int.* **55**, 527–538 (1990).
99. Pratt, R. G. Inverse theory applied to multi-source cross-hole tomography. Part II: Elastic wave-equation method. *Geophys. Prospecting* **38**, 311–330 (1990).
Application and evaluation of frequency-domain FWI in exploration seismology.
100. Komatitsch, D. & Vilotte, J. P. The spectral-element method: an efficient tool to simulate the seismic response of 2D and 3D geological structures. *Bull. Seism. Soc. Am.* **88**, 368–392 (1998).
101. Komatitsch, D. & Tromp, J. Introduction to the spectral-element method for 3-D seismic wave propagation. *Geophys. J. Int.* **139**, 806–822 (1999).
102. Komatitsch, D. & Tromp, J. Spectral-element simulations of global seismic wave propagation-I. Validation. *Geophys. J. Int.* **149**, 390–412 (2002).
103. Komatitsch, D. & Tromp, J. Spectral-element simulations of global seismic wave propagation-II. 3-D models, oceans, rotation, and self-gravitation. *Geophys. J. Int.* **150**, 303–318 (2002).
104. Afanasiev, M. et al. Modular and flexible spectral-element waveform modelling in two and three dimensions. *Geophys. J. Int.* **216**, 1675–1692 (2019).
105. Tarantola, A. *Inverse Problem Theory and Methods for Model Parameter Estimation* (Society for Industrial and Applied Mathematics, 2005).
106. Métivier, L., Brossier, R., Mérigot, Q., Oudet, E. & Virieux, J. Measuring the misfit between seismograms using an optimal transport distance: application to full waveform inversion. *Geophys. J. Int.* **205**, 345–377 (2016).
107. Park, J., Lindberg, C. R. & Vernon III, F. L. Multitaper spectral analysis of high-frequency seismograms. *J. Geophys. Res.* **92**, 12675–12684 (1987).
108. Laske, G. & Masters, G. Constraints on global phase velocity maps from long-period polarization data. *J. Geophys. Res.* **101**, 16059–16075 (1996).
109. Ekström, G., Tromp, J. & Larson, E. Measurements and global models of surface wave propagation. *J. Geophys. Res.* **102**, 8137–8157 (1997).
110. Fichtner, A., Kennett, B. L. N., Igel, H. & Bunge, H. P. Theoretical background for continental- and global-scale full-waveform inversion in the time-frequency domain. *Geophys. J. Int.* **175**, 665–685 (2008).
111. Bozdağ, E., Trampert, J. & Tromp, J. Misfit functions for full waveform inversion based on instantaneous phase and envelope measurements. *Geophys. J. Int.* **185**, 845–870 (2011).
112. Yuan, Y., Simons, F. & Tromp, J. Double-difference adjoint seismic tomography. *Geophys. J. Int.* **206**, 1599–1618 (2016).
113. Shin, C. & Min, D.-J. Waveform inversion using a logarithmic wavefield. *Geophysics* **71**, R31–R42 (2006).
114. Shin, C., Pyun, S. & Bednar, J. B. Waveform inversion using a logarithmic wavefield. *Geophys. Prospecting* **55**, 449–464 (2007).
115. Shin, C. & Cha, Y. H. Waveform inversion in the Laplace domain. *Geophys. J. Int.* **173**, 922–931 (2008).
116. Shin, C. & Cha, Y. H. Waveform inversion in the Laplace–Fourier domain. *Geophys. J. Int.* **177**, 1067–1079 (2009).
117. Warner, M. & Guasch, L. Adaptive waveform inversion: theory. *Geophysics* **81**, R429–R445 (2018).
118. Ramos-Martínez, J., Qiu, L., Valenciano, A. A., Jiang, X. & Chemingui, N. Long-wavelength FWI updates in the presence of cycle skipping. *Lead. Edge* **38**, 193–196 (2019).
119. Huang, G., Nammour, R. & Symes, W. Full-waveform inversion via source-receiver extension. *Geophysics* **82**, R153–R171 (2017).
120. Biondi, B. & Almomin, A. Simultaneous inversion of full data bandwidth by tomographic full-waveform inversion. *Geophysics* **79**, WA129–WA140 (2014).
121. Engquist, B. & Froese, B. Application of the Wasserstein metric to seismic signals. *Commun. Math. Science* **12**, 979–988 (2014).
122. Yang, Y. & Engquist, B. Analysis of optimal transport and related misfit functions in full-waveform inversion. *Geophysics* **83**, A7–A12 (2018).
123. Métivier, L., Brossier, R., Mérigot, Q. & Oudet, E. A graph space optimal transport distance as a generalization of L p distances: application to a seismic imaging inverse problem. *Inverse Probl.* **35**, 085001 (2019).
124. van Leeuwen, T. & Herrmann, F. Mitigating local minima in full-waveform inversion by expanding the search space. *Geophys. J. Int.* **195**, 661–667 (2013).

125. Wang, C., Yingst, D., Farmer, P. & Leveille, J. Full-waveform inversion with the reconstructed wavefield method. *Geophysics* **81**, 1237–1241 (2016).
126. Anderson, J., Tan, L. & Wang, D. Time-reversal checkpointing methods for RTM and FWI. *Geophysics* **77**, S93–S103 (2012).
127. Komatitsch, D. et al. Anelastic sensitivity kernels with parsimonious storage for adjoint tomography and full waveform inversion. *Geophys. J. Int.* **206**, 1467–1478 (2016).
128. Akçelik, V. *Multiscale Newton-Krylov Methods for Inverse Acoustic Wave Propagation*. Thesis, Carnegy-Mellon Univ. (2002).
129. Plessix, R.-E. Three-dimensional frequency-domain full-waveform inversion with an iterative solver. *Geophysics* **74**, WCC53–WCC61 (2009).
130. Operto, S. et al. Efficient 3-D frequency-domain mono-parameter full-waveform inversion of ocean-bottom cable data: application to Valhall in the visco-acoustic vertical transverse isotropic approximation. *Geophys. J. Int.* **202**, 1362–1391 (2015).
131. Operto, S. & Miniussi, A. On the role of density and attenuation in three-dimensional multiparameter viscoacoustic VTI frequency-domain FWI: an OBC case study from the North Sea. *Geophys. J. Int.* **213**, 2037–2059 (2018).
132. Komatitsch, D., Tsuboi, S., Ji, C. & Tromp, J. A 14.6 billion degrees of freedom, 5 teraflops, 2.5 terabyte earthquake simulation on the Earth Simulator. *Proc. 2003 ACM/IEEE Conf. Supercomputing* **1**, 4–11 (2003).
133. Peter, D. et al. Forward and adjoint simulations of seismic wave propagation on fully unstructured hexahedral meshes. *Geophys. J. Int.* **186**, 721–739 (2011).
134. Gunzburger, M. *Perspectives in Flow Control and Optimization* (SIAM, 2000).
135. Pratt, R. G., Shin, C. & Hicks, G. J. Gauss-Newton and full Newton methods in frequency-space seismic waveform inversion. *Geophys. J. Int.* **133**, 341–362 (1998).
136. Akçelik, V., Biros, G. & Ghattas, O. Parallel multiscale Gauss–Newton–Krylov methods for inverse wave propagation. *Proc. 2002 ACM/IEEE Conf. Supercomputing* 1–15 (2002).
137. Akçelik, V. et al. in *Proceedings of the 2003 ACM/IEEE Conference on Supercomputing 52* https://doi.org/10.1145/1048935.1050202 (2003).
138. Burstedde, C. & Ghattas, O. Algorithmic strategies for full waveform inversion: 1D experiments. *Geophysics* **74**, WCC37–W3346 (2009).
139. Modrak, R. & Tromp, J. Seismic waveform inversion best practices: regional, global and exploration test cases. *Geophys. J. Int.* **206**, 1864–1889 (2016).
140. Liu, D. & Nocedal, J. On the limited memory BFGS method for large scale optimization. *Math. Program.* **45**, 504–528 (1989).
141. Nash, S. & Nocedal, J. A numerical study of the limited memory BFGS method and the truncated-Newton method for large scale optimization. *SIAM J. Optim.* **1**, 358–372 (1991).
142. Zou, X. et al. Numerical experience with limited-memory quasi-Newton and truncated Newton methods. *SIAM J. Optim.* **3**, 582–608 (1993).
143. Nocedal, J. Theory of algorithms for unconstrained optimization. *Acta Numerica* **1**, 199–242 (1992).
144. Koren, Z., Mosegaard, K., Landa, E., Thore, P. & Tarantola, A. Monte Carlo estimation and resolution analysis of seismic background velocities. *J. Geophys. Res.* **96**, 20289–20299 (1991).
145. Mosegaard, K. & Tarantola, A. Monte Carlo sampling of solutions to inverse problems. *J. Geophys. Res.* **100**, 12431–12447 (1995).
146. Sambridge, M. & Mosegaard, K. Monte Carlo methods in geophysical inverse problems. *Rev. Geophys.* **40**, 1–29 (2002).
147. Fichtner, A., Zunino, A. & Gebraad, L. Hamiltonian Monte Carlo solution of tomographic inverse problems. *Geophys. J. Int.* **216**, 1344–1363 (2019).
148. Sengupta, M. & Toksöz, N. Three-dimensional model of seismic velocity variation in the Earth's mantle. *Geophys. Res. Lett.* **3**, 84–86 (1977).
149. Claerbout, J. F. Toward a unified theory of reflector mapping. *Geophysics* **36**, 467–481 (1971).
150. Claerbout, J. & Doherty, S. Downward continuation of moveout-corrected seismograms. *Geophysics* **37**, 741–768 (1972).
151. Aki, K. & Richards, P. G. *Quantitative Seismology, Theory and Methods* (W. H. Freeman, 1980).
152. Montagner, J.-P. & Jobert, N. Vectorial tomography; II. Application to the Indian Ocean. *Geophys. J.* **94**, 309–344 (1988).
153. Marone, F. & Romanowicz, B. Non-linear crustal corrections in high-resolution regional waveform seismic tomography. *Geophys. J. Int.* **170**, 460–467 (2007).
154. Schneider, W. A. Integral formulation for migration in two and three dimensions. *Geophysics* **43**, 49–76 (1978).
155. Baysal, E., Kosloff, D. & Sherwood, J. Reverse time migration. *Geophysics* **48**, 1514–1524 (1983).
156. Hill, N. R. Gaussian beam migration. *Geophysics* **55**, 1416–1428 (1990).
157. Stolt, R. H. Migration by Fourier transform. *Geophysics* **43**, 23–48 (1978).
158. Gazdag, J. Wave equation migration with the phase-shift method. *Geophysics* **43**, 1342–1351 (1978).
159. Aki, K. Space and time spectra of stationary stochastic waves, with special reference to microtremors. *Bull. Earthq. Res. Inst.* **35**, 415–456 (1957).
160. Claerbout, J. F. Synthesis of a layered medium from its acoustic transmission response. *Geophysics* **33**, 264–269 (1968).
161. Fichtner, A. & Tsai, V. C. Theoretical foundations of noise interferometry. in *Seismic Ambient Noise* (eds Nakata, N., Gualtieri, L. & Fichtner, A.) 109–143 (Cambridge Univ. Press, 2019).
162. Sirgue, L. et al. Full waveform inversion: the next leap forward in imaging at Valhall. *First Break* **28**, 65–70 (2010).
163. Barkved, O. et al. in *Expanded Abstracts, 91st Annual SEG Meeting and Exposition (October 17–22, Denver)* 925–929 (Society of Exploration Geophysics, 2010).
164. Amestoy, P. et al. Fast 3D frequency-domain full waveform inversion with a parallel block low-rank multifrontal direct solver: application to OBC data from the North Sea. *Geophysics* **81**, R363–R383 (2016).
165. Operto, S. et al. Computationally-efficient three-dimensional visco-acoustic finite-difference frequency-domain seismic modeling in vertical transversely isotropic media with sparse direct solver. *Geophysics* **79**, T257–T275 (2014).
166. Kurzmann, A., Przebindowska, A., Kohn, D. & Bohlen, T. Acoustic full waveform tomography in the presence of attenuation: a sensitivity analysis. *Geophys. J. Int.* **195**, 985–1000 (2013).
167. Operto, S. et al. A guided tour of multiparameter full-waveform inversion with multicomponent data: from theory to practice. *Lead. Edge* **32**, 1040–1054 (2013).
168. Luo, Y., Modrak, R. & Tromp, J. in *Handbook of Geomathematics* 2nd edn (eds Freeden, W., Nahed, Z. & Sonar, T.) 1–52 (Springer, 2014).
169. Roecker, S., Baker, B. & McLaughlin, J. A finite-difference algorithm for full waveform teleseismic tomography. *Geophys. J. Int.* **181**, 1017–1040 (2010).
170. Monteiller, V., Chevrot, S., Komatitsch, D. & Fuji, N. A hybrid method to compute short-period synthetic seismograms of teleseismic body waves in a 3-D regional model. *Geophys. J. Int.* **192**, 230–247 (2013).
171. Monteiller, V., Chevrot, S., Komatitsch, D. & Wang, Y. Three-dimensional full waveform inversion of short-period teleseismic wavefields based upon the SEM-DSM hybrid method. *Geophys. J. Int.* **202**, 811–827 (2015).
172. Tong, P., Chen, C. W., Komatitsch, D., Basini, P. & Liu, Q. High-resolution seismic array imaging based on an SEM-FK hybrid method. *Geophys. J. Int.* **197**, 369–395 (2014).
173. Tong, P. et al. A 3-D spectral-element and frequency-wave number hybrid method for high-resolution seismic array imaging. *Geophys. Res. Lett.* **41**, 7025–7034 (2014).
174. Masson, Y. & Romanowicz, B. Box tomography: Localised imaging of remote targets buried in an unknown medium, a step forward for understanding key structures in the deep Earth. *Geophys. J. Int.* **211**, 141–163 (2017).
175. Wang, Y. et al. The deep roots of the western Pyrenees revealed by full waveform inversion of teleseismic P waves. *Geology* **44**, 475–478 (2016).
176. Beller, S. et al. Lithospheric architecture of the South-Western Alps revealed by multiparameter teleseismic full-waveform inversion. *Geophys. J. Int.* **212**, 1369–1388 (2018).
177. Clouzet, P., Masson, Y. & Romanowicz, B. Box Tomography: first application to the imaging of upper-mantle shear velocity and radial anisotropy structure beneath the North American continent. *Geophys. J. Int.* **213**, 1849–1875 (2018).
178. Chevrot, S. & Sylvander, M. Maupasacq. International Federation of Digital Seismograph Networks. Dataset/Seismic Network. 10.7914/SN/XD_2017 (2017).
179. Polychronopoulou, K. et al. Broadband, short-period or geophone nodes? Quality assessment of passive seismic signals acquired during the Maupasacq experiment. *First Break* **36**, 71–75 (2018).
180. Fichtner, A. et al. The deep structure of the North Anatolian Fault Zone. *Earth Planet. Sci. Lett.* **373**, 109–117 (2013).
181. Colli, L., Fichtner, A. & Bunge, H.-P. Full waveform tomography of the upper mantle in the South Atlantic region: imaging a westward fluxing shallow asthenosphere? *Tectonophysics* **604**, 26–40 (2013).
182. Zhu, H. & Tromp, J. Mapping tectonic deformation in the crust and upper mantle beneath Europe and the North Atlantic Ocean. *Science* **341**, 871–875 (2013).
Continental-scale horizontal transverse isotropy FWI of the European crust and upper mantle.
183. Zhu, H., Bozdağ, E., Duffy, T. & Tromp, J. Seismic attenuation beneath Europe and the North Atlantic: Implications for water in the mantle. *Earth Planet. Sci. Lett.* **381**, 1–11 (2013).
184. Zhu, H., Bozdağ, E. & Tromp, J. Seismic structure of the European upper mantle based on adjoint tomography. *Geophys. J. Int.* **201**, 18–52 (2015).
185. Rickers, F., Fichtner, A. & Trampert, J. The Iceland–Jan Mayen plume system and its impact on mantle dynamics in the North Atlantic region: Evidence from full-waveform inversion. *Earth Planet. Sci. Lett.* **367**, 39–51 (2013).
186. Fichtner, A. & Villaseñor, A. Crust and upper mantle of the western Mediterranean – Constraints from full-waveform inversion. *Earth Planet. Sci. Lett.* **428**, 52–62 (2015).
187. Çubuk Sabuncu, Y., Taymaz, T. & Fichtner, A. 3-D crustal velocity structure of western Turkey: Constraints from full-waveform tomography. *Phys. Earth Planet. Inter.* **270**, 90–112 (2017).
188. Zhu, H., Komatitsch, D. & Tromp, J. Radial anisotropy of the North American upper mantle based on adjoint tomography with USArray. *Geophys. J. Int.* **211**, 349–377 (2017).
189. Krischer, L., Fichtner, A., Boehm, C. & Igel, H. Automated large-scale full seismic waveform inversion for North America and the North Atlantic. *J. Geophys. Res.* **123**, 5902–5928 (2018).
190. Chen, M., Niu, F., Liu, Q., Tromp, J. & Zheng, X. Multiparameter adjoint tomography of the crust and upper mantle beneath East Asia: 1. Model construction and comparisons. *J. Geophys. Res.* **120**, 1762–1786 (2015).
191. Simutė, S., Steptoe, H., Cobden, L. J., Gokhberg, A. & Fichtner, A. Full-waveform inversion of the Japanese Islands region. *J. Geophys. Res.* **121**, 3722–3741 (2016).
192. Tao, K., Grand, S. & Niu, F. Seismic structure of the upper mantle beneath eastern Asia from full waveform seismic tomography. *Geochem. Geophys. Geosyst.* **19**, 2732–2763 (2018).
193. Lloyd, A. et al. Radially anisotropic seismic structure of the Antarctic upper mantle based on full-waveform adjoint tomography. *Geophys. J. Int*. (in the press).
194. Capdeville, Y., Chaljub, E. & Montagner, J. P. Coupling the spectral element method with a modal solution for elastic wave propagation in global earth models. *Geophys. J. Int.* **152**, 34–67 (2003).
195. Li, X.-D. & Romanowicz, B. Global mantle shear velocity model developed using nonlinear asymptotic coupling theory. *J. Geophys. Res.* **101**, 22245–22272 (1996).
196. French, S. W. & Romanowicz, B. Whole-mantle radially anisotropic shear velocity structure from spectral-element waveform tomography. *Geophys. J. Int.* **199**, 1303–1327 (2014).
197. Valentine, A. & Trampert, J. The impact of approximations and arbitrary choices on geophysical images. *Geophys. J. Int.* **204**, 59–73 (2016).
198. Fichtner, A. et al. Multi-scale full waveform inversion. *Geophys. J. Int.* **194**, 534–556 (2013).
199. Afanasiev, M. et al. Foundations for a multiscale collaborative global Earth model. *Geophys. J. Int.* **204**, 39–58 (2016).
200. Fichtner, A. et al. The collaborative seismic earth model: generation 1. *Geophys. Res. Lett.* **45**, 4007–4016 (2019).
201. Fukao, Y. & Obayashi, M. Subducted slabs stagnant above, penetrating through, and trapped below the 660 km discontinuity. *J. Geophys. Res.* **118**, 5920–5938 (2013).

202. Van der Meer, D. G., Van Hinsbergen, D. J. & Spakman, W. Atlas of the underworld: Slab remnants in the mantle, their sinking history, and a new outlook on lower mantle viscosity. *Tectonophysics* **723**, 309–448 (2018).
203. Grand, S. P. Mantle shear structure beneath the Americas and surrounding oceans. *J. Geophys. Res.* **99**, 11591–11621 (1994).
204. Fukao, Y., Obayashi, M., Inoue, H. & Nenbai, M. Subducting slabs stagnant in the mantle transition zone. *J. Geophys. Res.* **97**, 4809–4822 (1992).
205. Su, W., Woodward, R. & Dziewonski, A. Degree 12 model of shear velocity heterogeneity in the mantle. *J. Geophys. Res.* **99**, 6945–6980 (1994).
206. Ruan, Y. et al. Balancing unevenly distributed data in seismic tomography: a global adjoint tomography example. *Geophys. J. Int.* **219**, 1225–1236 (2019).
207. Pratt, R. G., Plessix, R. E. & Mulder, W. A. in *63rd EAGE Conf. Exhibition* P092 (SEAGE, 2001).
208. Pratt, R. G., Sirgue, L., Hornby, B. & Wolfe, J. in *70th EAGE Conf. Exhibition incorporating SPE EUROPEC 2008* F020 (2008).
209. Gholami, Y., Brossier, R., Operto, S., Ribodetti, A. & Virieux, J. Which parametrization is suitable for acoustic VTI full waveform inversion? *Geophysics* **78**, R81–R105 (2013).
210. Smith, M. & Dahlen, F. The azimuthal dependence of Love and Rayleigh wave propagation in a slightly anisotropic medium. *J. Geophys. Res.* **78**, 3321–3333 (1973).
211. Montagner, J.-P. & Nataf, H. A simple method for inverting the azimuthal anisotropy of surface waves. *J. Geophys. Res.* **91**, 511–520 (1986).
212. Duveneck, E. & Bakker, P. M. Stable P-wave modeling for reverse-time migration in tilted TI media. *Geophysics* **76**, S65–S75 (2011).
213. Oropeza, E. & McMechan, G. A. Common-reflection-point migration velocity analysis of 2D P-wave data from TTI media. *Geophysics* **79**, C65–C79 (2014).
214. Rusmanugroho, H., Modrak, R. & Tromp, J. Anisotropic full-waveform inversion with tilt-angle recovery. *Geophysics* **82**, R135–R151 (2017).
215. Liao, Q. & McMechan, G. A. 2.5D full-wavefield viscoacoustic inversion. *Geophys. Prospecting* **43**, 1043–1059 (1995).
216. Song, Z., Williamson, P. & Pratt, G. Frequency-domain acoustic-wave modeling and inversion of crosshole data, Part 2: Inversion method, synthetic experiments and real-data results. *Geophysics* **60**, 786–809 (1995).
217. Hicks, G. J. & Pratt, R. G. Reflection waveform inversion using local descent methods: Estimating attenuation and velocity over a gas-sand deposit. *Geophysics* **66**, 598–612 (2001).
218. Prieux, V., Brossier, R., Operto, S. & Virieux, J. Multiparameter full waveform inversion of multicomponent ocean-bottom-cable data from the Valhall field. Part 1: Imaging compressional wave speed, density and attenuation. *Geophys. J. Int.* **194**, 1640–1664 (2013).
219. Yuan, Y. O., Simons, F. J. & Bozdağ, E. Multiscale adjoint waveform tomography for surface and body waves. *Geophysics* **80**, R281–R302 (2015).
220. Blom, N., Boehm, C. & Fichtner, A. Synthetic inversions for density using seismic and gravity data. *Geophys. J. Int.* **209**, 1204–1220 (2017).
221. Bernauer, M., Fichtner, A. & Igel, H. Optimal observables for multiparameter seismic tomography. *Geophys. J. Int.* **198**, 1241–1254 (2014).
222. Modrak, R. T., Borisov, D., Lefebvre, M. & Tromp, J. Seisflows – flexible waveform inversion software. *Comput. Geosci.* **115**, 88–95 (2018).
223. Balasubramanian, V. et al. in *2018 IEEE International Parallel and Distributed Processing Symposium (IPDPS)* 536–545 (IEEE, 2018).
224. Lefebvre, M. et al. in *Exascale Scientific Applications — Scalability and Performance Portability* (eds Straatsma, T., Antypas, K. & Williams, T.) (CRC, 2018).
225. Liu, Q. et al. Hello ADIOS: the challenges and lessons of developing leadership class I/O frameworks. *Concurr. Comput. Pract. Exp.* **26**, 1453–1473 (2014).
226. Boehm, C., Hanzich, M., de la Puente, J. & Fichtner, A. Wavefield compression for adjoint methods in full-waveform inversion. *Geophysics* **81**, R385–R397 (2016).
227. Krischer, L. et al. An adaptable seismic data format. *Geophys. J. Int.* **207**, 1003–1011 (2016).
228. Maggi, A., Tape, C., Chen, M., Chao, D. & Tromp, J. An automated time-window selection algorithm for seismic tomography. *Geophys. J. Int.* **178**, 257–281 (2009).
229. Chen, Y. et al. Automated time-window selection based on machine learning for full-waveform inversion. *SEG Technical Program Expanded Abstracts* 1604–1609 (2017).
230. Rawlinson, N., Fichtner, A., Sambridge, M. & Young, M. K. Seismic tomography and the assessment of uncertainty. *Adv. Geophysics* **55**, 1–76 (2014).
231. Fichtner, A. & Trampert, J. Hessian kernels of seismic data functionals based upon adjoint techniques. *Geophys. J. Int.* **185**, 775–798 (2011).
232. Fichtner, A. & Trampert, J. Resolution analysis in full waveform inversion. *Geophys. J. Int.* **187**, 1604–1624 (2011).
233. Zhu, H., Li, S., Fomel, S., Städler, G. & Ghattas, O. A Bayesian approach to estimate uncertainty for full-waveform inversion using a priori information from depth migration. *Geophysics* **81**, R307–R323 (2016).
234. Fichtner, A. & van Leeuwen, T. Resolution analysis by random probing. *J. Geophys. Res.* **120**, 5549–5573 (2015).
235. Fang, Z., Silva, C., Kuske, R. & Herrmann, F. Uncertainty quantification for inverse problems with weak partial-differential-equation constraints. *Geophysics* **83**, R629–R647 (2018).
236. Thurin, J., Brossier, R. & Métivier, L. Ensemble-based uncertainty estimation in full waveform inversion. *Geophys. J. Int.* **219**, 1613–1635 (2019).
237. Eikrem, K. S., Nævdal, G. & Jacobsen, M. Iterated extended Kalman filter method for time-lapse seismic full-waveform inversion. *Geophys. Prospecting* **67**, 379–394 (2019).
238. Liu, Q., Peter, D. & Tape, C. Square-root variable metric based elastic full-waveform inversion – Part 1: theory and validation. *Geophys. J. Int.* **218**, 1121–1135 (2019).
239. Liu, Q. & Peter, D. Square-root variable metric based elastic full-waveform inversion – Part 2: uncertainty estimation. *Geophys. J. Int.* **218**, 1100–1120 (2019).
240. Martin, G., Wiley, R. & Marfurt, K. Marmousi2: an elastic upgrade for Marmousi. *Lead. Edge* **25**, 156–166 (2006).
241. Plessix, R.-É. Three-dimensional frequency-domain full-waveform inversion with an iterative solver. *Geophysics* **74**, WCC149–WCC157 (2009).
242. Krebs, J. et al. Fast full-wavefield seismic inversion using encoded sources. *Geophysics* **74**, WCC177–WCC188 (2009).
243. Ben-Hadj-Ali, H., Operto, S. & Virieux, J. An efficient frequency-domain full waveform inversion method using simultaneous encoded sources. *Geophysics* **76**, R109–R124 (2009).
244. Choi, Y. & Alkhalifah, T. Source-independent time-domain wave-form inversion using convolved wavefields. *Geophysics* **76**, R125–R134 (2011).
245. Schuster, G., Wang, X., Huang, Y., Dai, W. & Boonyasiriwat, C. Theory of multisource crosstalk reduction by phase-encoded statics. *Geophys. J. Int.* **184**, 1289–1303 (2011).
246. Schiemenz, A. & Igel, H. Accelerated 3-D full-waveform inversion using simultaneously encoded sources in the time domain: application to Valhall ocean-bottom cable data. *Geophys. J. Int.* **195**, 1970–1988 (2013).
247. Castellanos, C., Métivier, L., Operto, S., Brossier, R. & Virieux, J. Fast full waveform inversion with source encoding and second-order optimization methods. *Geophys. J. Int.* **200**, 718–742 (2015).
248. Zhao, Z., Sen, M. & Stoffa, P. Double-plane-wave reverse time migration in the frequency domain. *Geophysics* **81**, S367–S382 (2016).
249. Romero, L., Ghiglia, D., Ober, C. & Morton, S. Phase encoding of shot records in prestack migration. *Geophysics* **65**, 426–436 (2000).
250. Krebs, J. R. et al. Orthogonal source and receiver encoding. US Patent 10,012,745) (2013).
251. Huang, Y. & Schuster, G. in *75th EAGE Conf. Exhibition incorporating SPE EUROPEC 2013* (2013).
252. Huang, Y. & Schuster, G. Full-waveform inversion with multisource frequency selection of marine streamer data. *Geophys. Prospecting* **66**, 1243–1257 (2018).
253. Zhang, Q., Mao, W., Zhou, H., Zhang, H. & Chen, Y. Hybrid-domain simultaneous-source full waveform inversion without crosstalk noise. *Geophys. J. Int.* **215**, 1659–1681 (2018).
254. Tromp, J. & Bachmann, E. Source encoding for adjoint tomography. *Geophys. J. Int.* **218**, 2019–2044 (2019).
255. Herrmann, F. J. Randomized sampling and sparsity: Getting more information from fewer samples. *Geophysics* **75**, WB173–WB187 (2009).
256. Herrmann, F. J. & Li, X. Efficient least-squares imaging with sparsity promotion and compressive sensing. *Geophys. Prospecting* **60**, 696–712 (2012).
257. Li, X., Aravkin, A. Y., van Leeuwen, T. & Herrmann, F. J. Fast randomized full-waveform inversion with compressive sensing. *Geophysics* **77**, A13–A17 (2012).
258. van Leeuwen, T. & Herrmann, F. J. Fast waveform inversion without source-encoding. *Geophys. Prospecting* **61**, 10–19 (2013).
259. Silva, C. D., Zhang, Y., Kumar, R. & Herrmann, F. J. Applications of low-rank compressed seismic data to full-waveform inversion and extended image volumes. *Geophysics* **84**, R371–R383 (2019).
260. Metropolis, N., Rosenbluth, A. W., Rosenbluth, M. N., Teller, A. H. & Teller, E. Equations of state calculations by fast computing machines. *J. Chem. Phys.* **21**, 1087–1092 (1953).
261. Hastings, W. K. Monte Carlo sampling methods using Markov chains and their applications. *Biometrika* **57**, 97–109 (1970).
262. Mosegaard, K. & Tarantola, A. Monte Carlo sampling of solutions to inverse problems. *J. Geophys. Res.* **100**, 431–447 (1995).
263. Wolpert, D. & Macready, W. G. No free lunch theorems for optimization. *IEEE Trans. Evolut. Comput.* **1**, 67–82 (1997).
264. Mosegaard, K. *Limits to Nonlinear Inversion* (Springer, 2012).
265. Bellman, R. E. *Dynamic Programming* (Rand Corporation, 1957).
266. Curtis, A. & Lomax, A. Prior information, sampling distributions, and the curse of dimensionality. *Geophysics* **66**, 372–378 (2001).
267. Kennedy, S. D. A. D., Pendleton, B. J. & Roweth, D. Hybrid Monte Carlo. *Phys. Lett. B* **195**, 216–222 (1987).
268. Neal, R. M. MCMC using Hamiltonian dynamics. in *Handbook of Markov Chain Monte Carlo* (eds Brooks, S., Gelman, A., Jones, G. & Meng, X.-L.) 113–162 (Chapman and Hall, 2011).
269. Betancourt, M. A conceptual introduction to Hamiltonian Monte Carlo. Preprint at *arXiv* https://arxiv.org/abs/1701.02434 (2017).
270. Fichtner, A. & Zunino, A. Hamiltonian nullspace shuttles. *Geophys. Res. Lett.* **46**, 644–651 (2019).

Acknowledgements

The author is grateful to S. Operto and S. Beller for their feedback and input on controlled-source seismology applications of full-waveform inversion and for contributing figures. W. Lei and Y. Ruan also contributed figures to this article. Comments and suggestions by the reviewers helped improve an earlier version of the manuscript. This research used the resources of the Oak Ridge Leadership Computing Facility, which is a US Department of Energy Office of Science User Facility supported under contract DE-AC05-00OR22725. Additional computational resources were provided by the Princeton Institute for Computational Science and Engineering (PICSciE).

Competing interests

The author declares no competing interests.

Peer review information

Nature Reviews Earth & Environment thanks A. Fichtner, B. Romanowicz and the other, anonymous, reviewer for their contribution to the peer review of this work.

Publisher's note

Springer Nature remains neutral with regard to jurisdictional claims in published maps and institutional affiliations.

RELATED LINKS

F-net: http://www.fnet.bosai.go.jp/top.php
GSN: https://www.iris.edu/hq/programs/gsn
Hi-net: http://www.hinet.bosai.go.jp/
MedNet: http://mednet.rm.ingv.it/earthquakes.php
QUEST: http://www.quest-itn.org
USArray: http://www.usarray.org/

© Springer Nature Limited 2019